Constraining models of particle acceleration by the variability analysis and imaging of relativistic jets

Łukasz Stawarz
Jagiellonian University

Polish-German WE-Heraeus-Seminar “The Variable Multi-Messenger Sky”, Kraków, November 2022

Blazar “one-zone” modeling

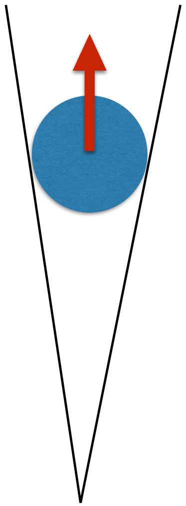

Blazar "one-zone" modeling

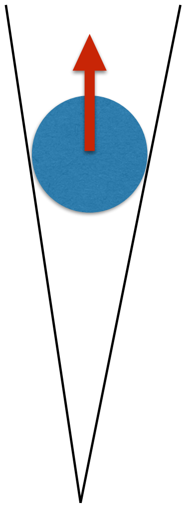

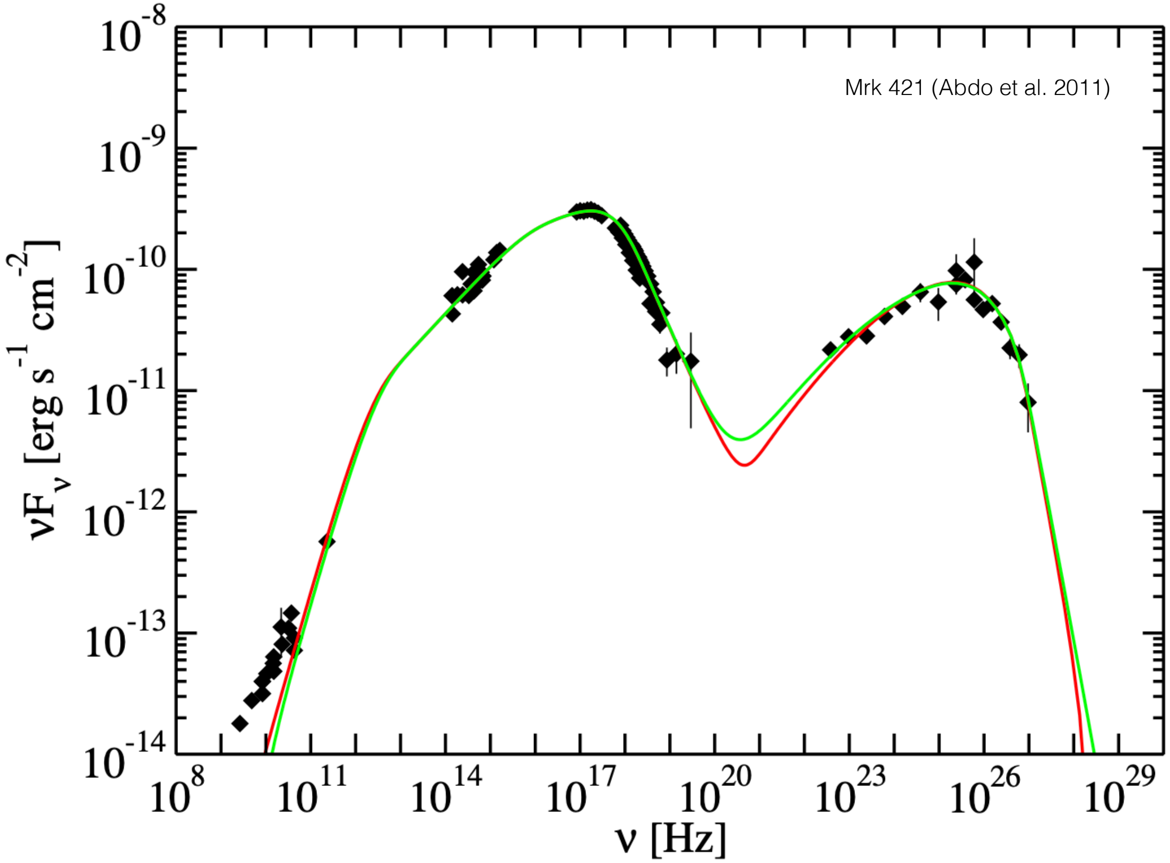

assumed steady-state electron spectrum

$$N_e(\gamma) \propto \begin{cases} \gamma^{-s_{\rm low}} & \text{for} \quad \gamma_{\rm min} < \gamma \le \gamma_{\rm br} \\ \gamma^{-s_{\rm high}} & \text{for} \quad \gamma_{\rm br} < \gamma \le \gamma_{\rm max} \end{cases}$$

Blazar MWL variability

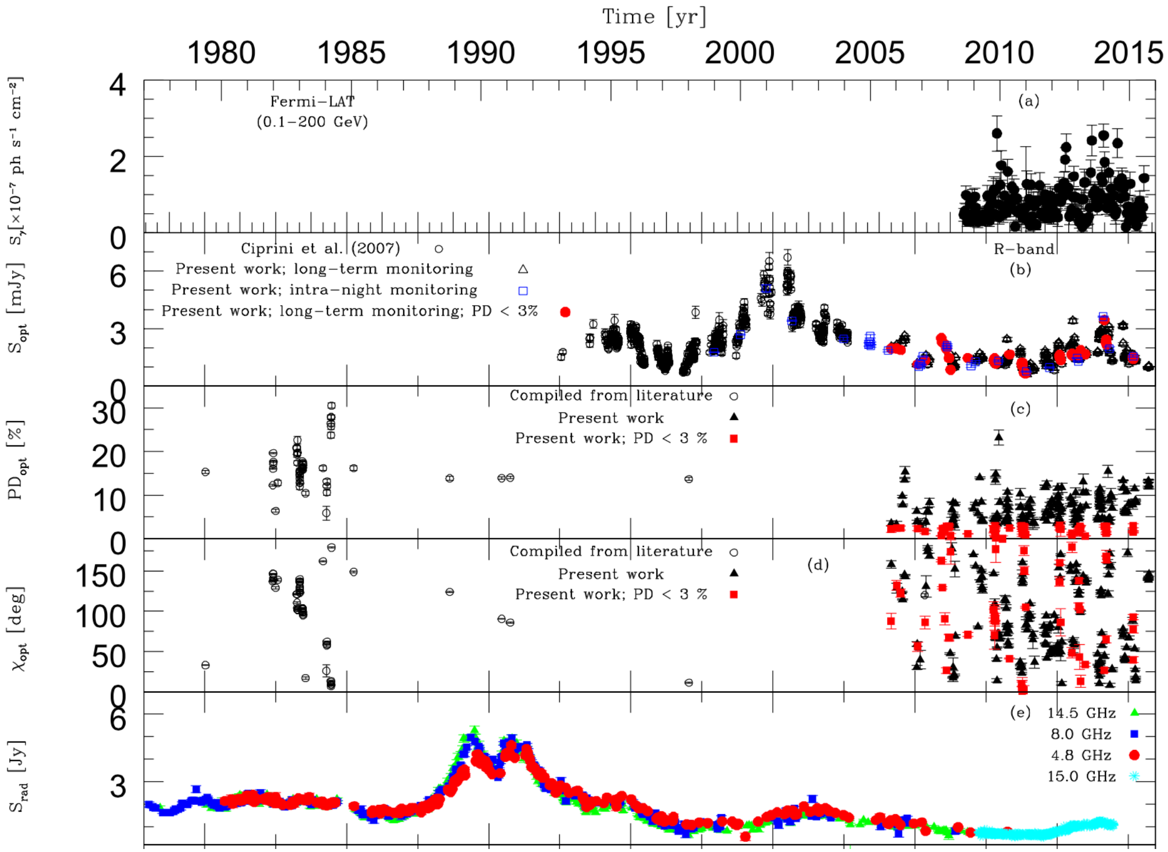

PKS 0735+178 (Goyal, LS, et al. 2017)

Blazar MWL variability

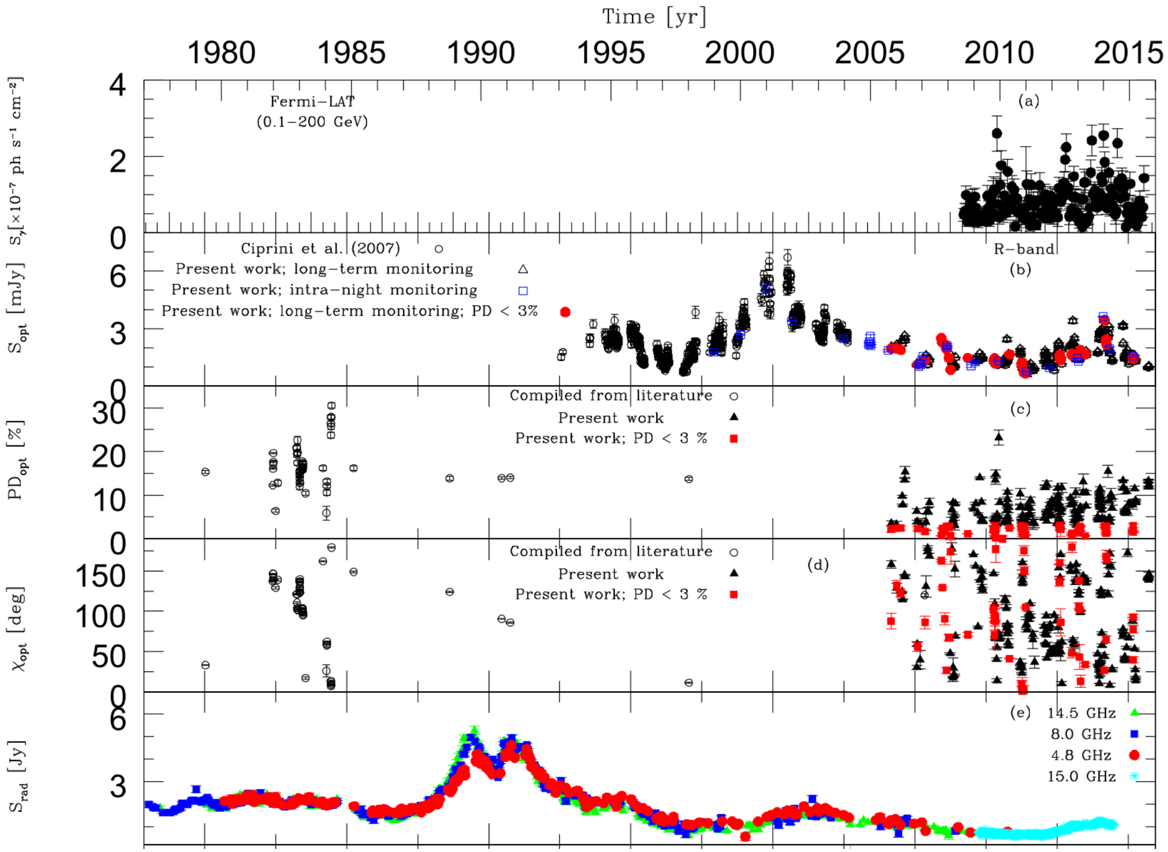

PKS 0735+178 (Goyal, LS, et al. 2017)

DFT

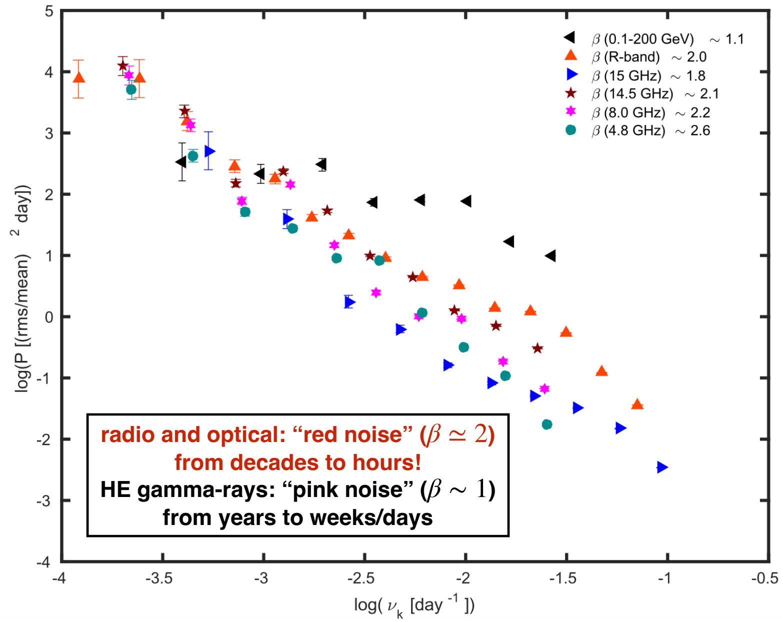

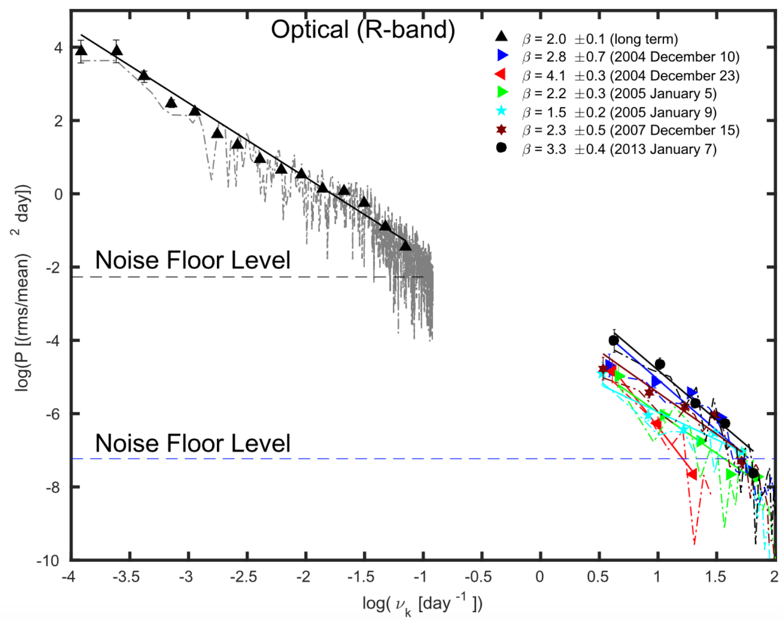

Blazar MWL variability

Power spectral density $P(f) \propto f^{-\beta}$

1) radio and optical ranges: “red noise” ($\beta \simeq 2$), from **tens of years to <u>hours</u>**!
2) gamma-rays: “pink noise” ($\beta \sim 1$) from years to weeks/days
3) X-rays in between red and pink noise, depending on a source
4) optical vs gamma-ray flux changes: comparable amplitudes on timescales of years; on shorter time scales “excess” gamma-ray variability

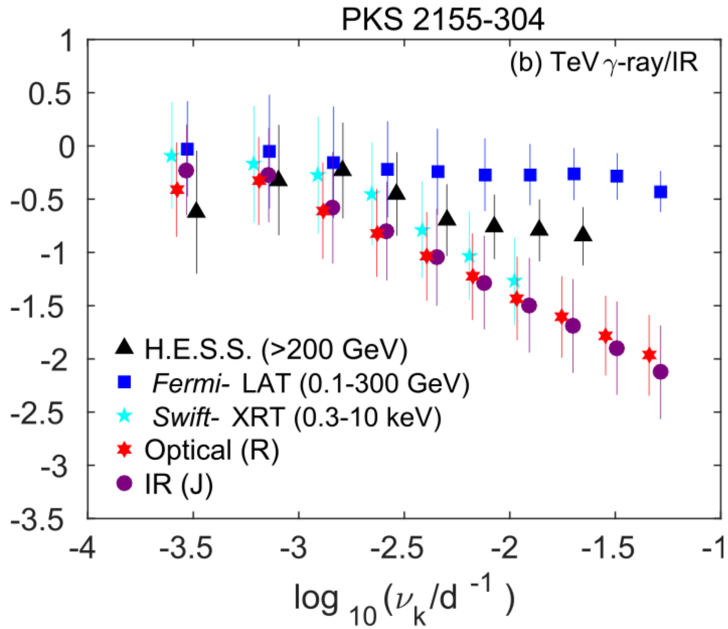

Magnetically Arrested Disks

O'Riordan et al. 2017:

"We show that this *[blazar]* variability can be produced by turbulence in relativistic jets launched by magnetically arrested accretion flows (MADs). We perform radiative transport calculations on the turbulent, highly magnetized jet launching region of a MAD with a rapidly rotating supermassive black hole. The resulting synchrotron and synchrotron self-Compton emission, originating from close to the black hole horizon, is highly variable. This variability is characterized by PDS, which is remarkably similar to the observed power-law spectrum at frequencies less than a few per day. Furthermore, turbulence in the jet launching region naturally produces fluctuations in the plasma on scales much smaller than the horizon radius. We speculate that similar turbulent processes, operating in the jet at large radii (and therefore a high bulk Lorentz factor), are responsible for blazar variability over many decades in frequency, including on minute timescales."

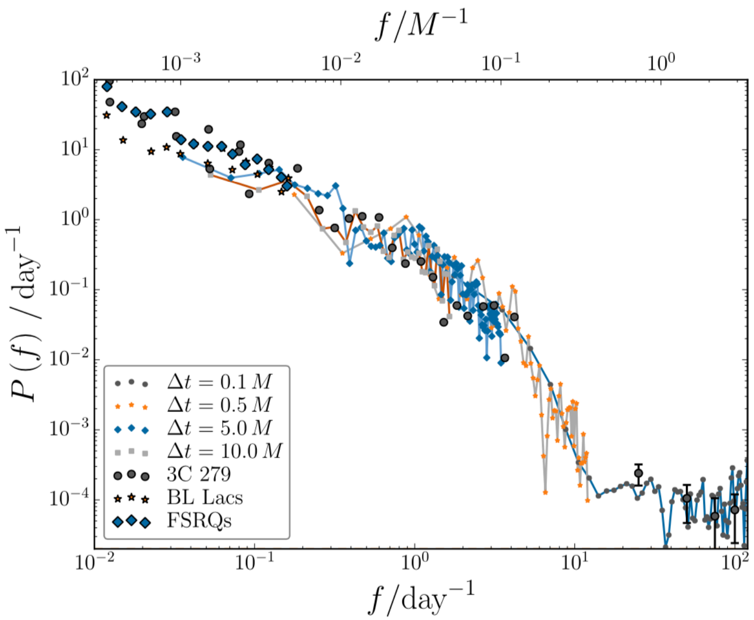

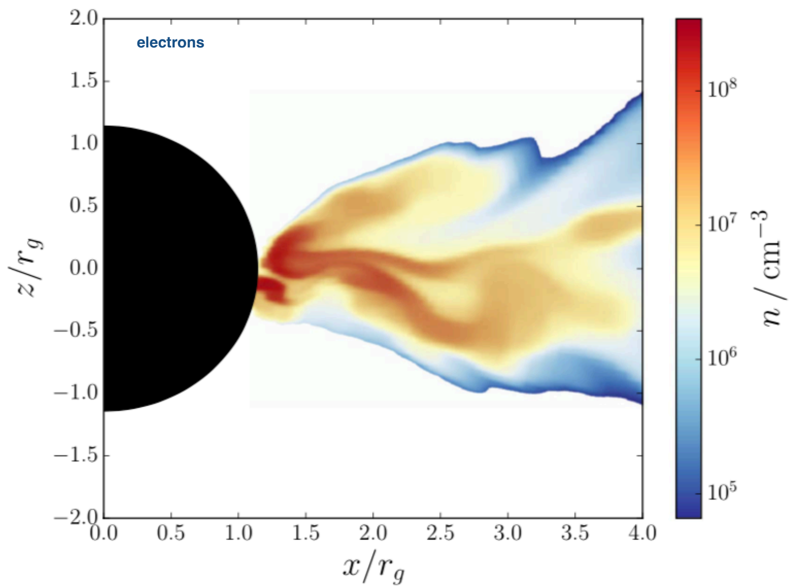

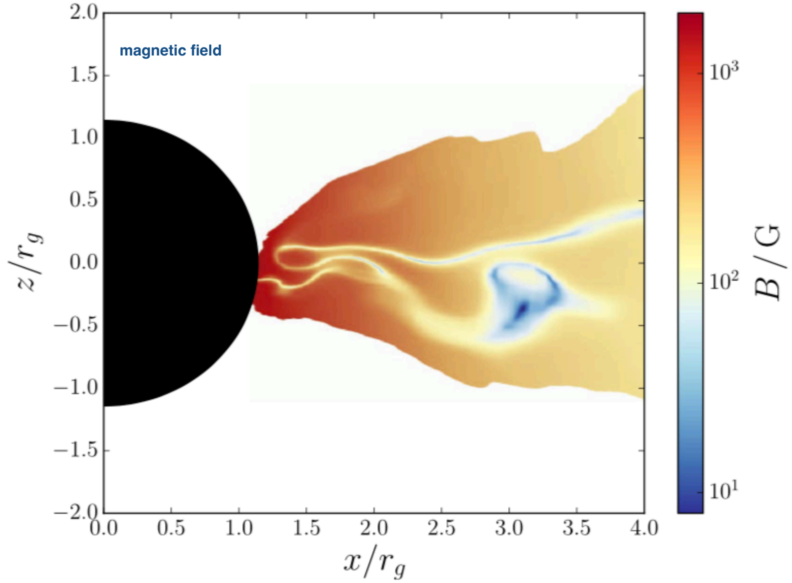

Jet-Disk Coupling

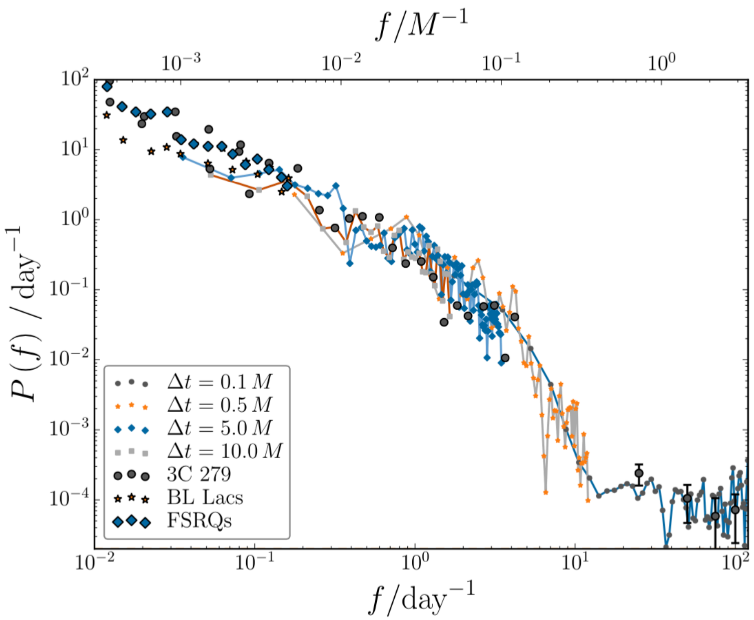

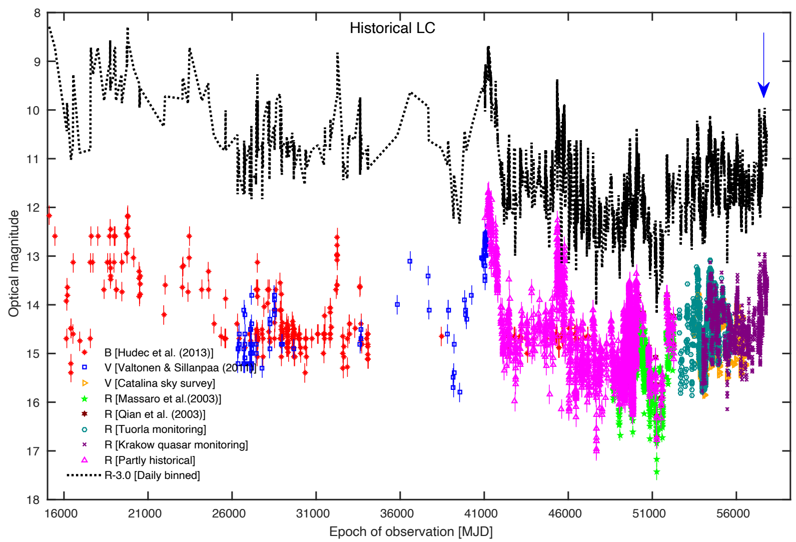

OJ287 (Goyal, LS, et al. 2018)

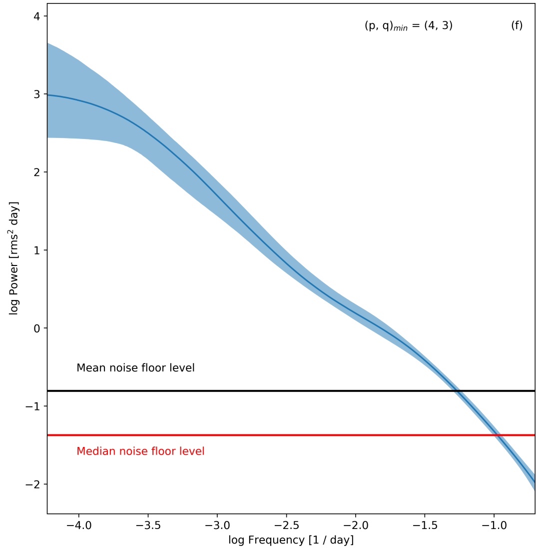

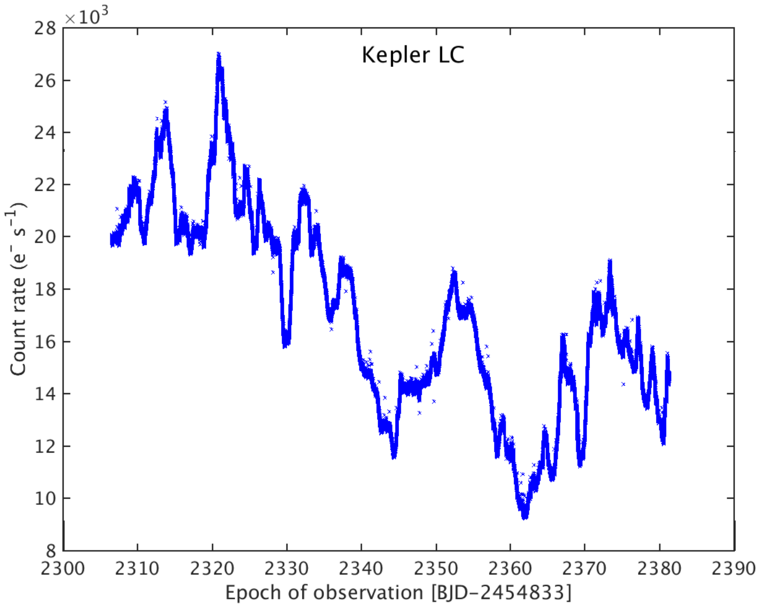

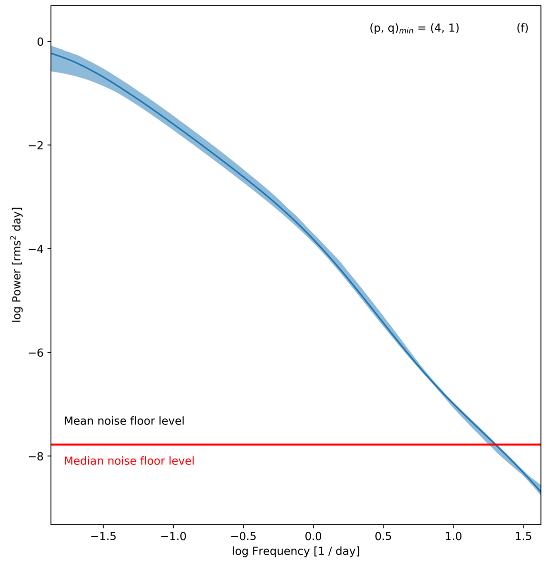

However…

…distorting effects due to the finite sampling of the lightcurve,
and irregular and/or sparse sampling

However…

…distorting effects due to the finite sampling of the lightcurve,
and irregular and/or sparse sampling

instead of standard Fourier decomposition methods, one can use a certain statistical model to fit the light curve in the time domain, and thus to derive the source power spectrum directly from the lightcurve, free from distortion effects (see Kelly et al. 2009 2011, 2014).

Ornstein-Uhlenbeck process, OU
Continuous time first order autoregressive process, CAR(1)
Damped Random Walk, DRW

$$dX(t) = -\omega_0(X(t) - \mu)dt + \varsigma dW(t), \quad \omega_0, \varsigma > 0$$

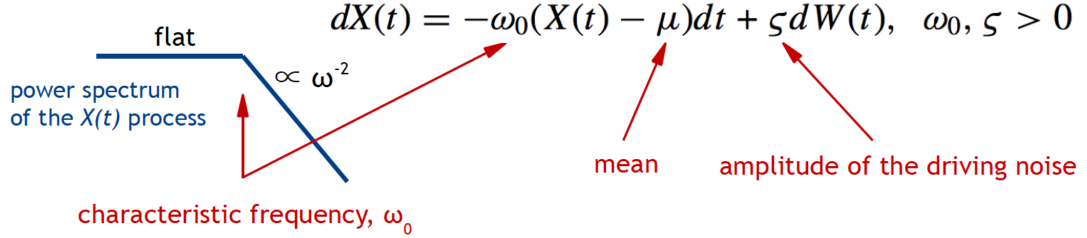

$$P_{\mathrm{OU}}(\omega) = \frac{\varsigma^2}{2\pi} \frac{1}{\omega_0^2 + \omega^2}$$

courtesy of M. Sobolewska

Stochastic model for Fermi-LAT blazar lightcurves

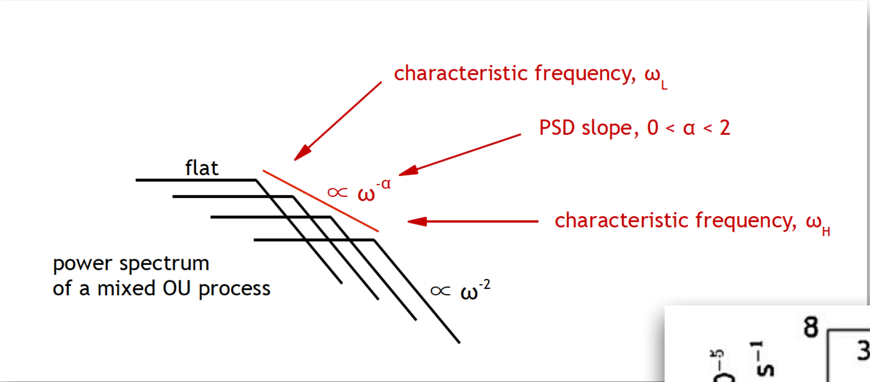

Sobolewska et al. 2014

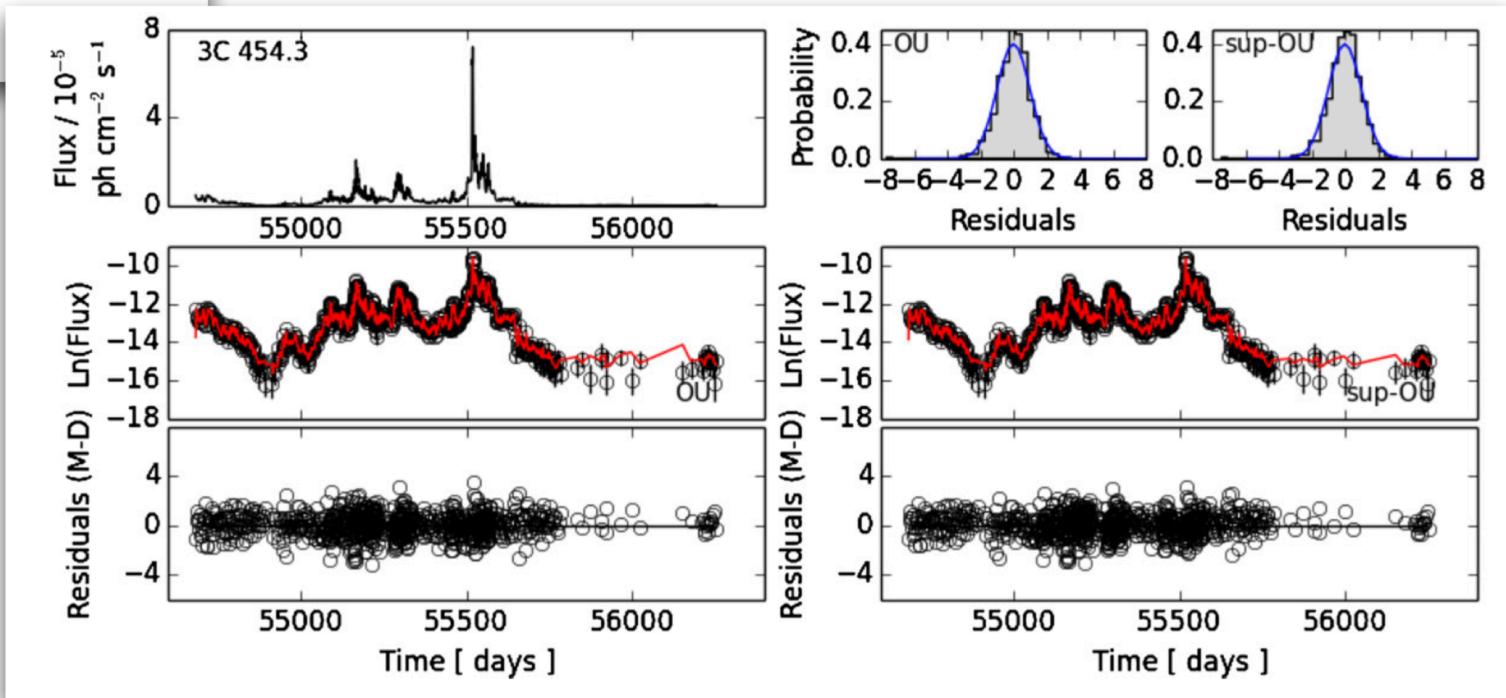

Stochastic model for Fermi-LAT blazar lightcurves

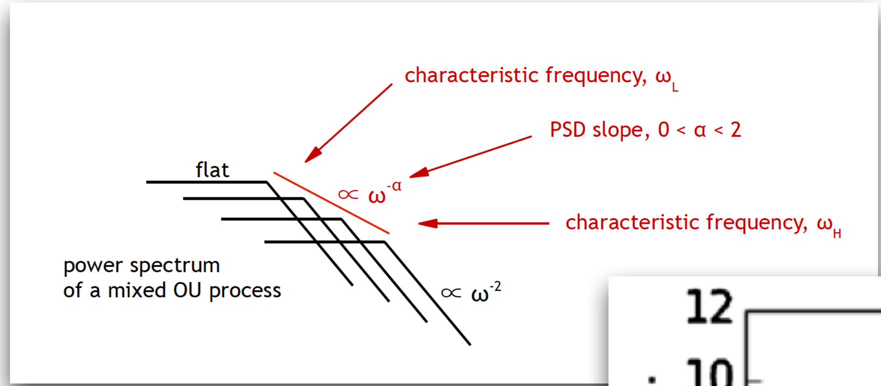

Sobolewska et al. 2014

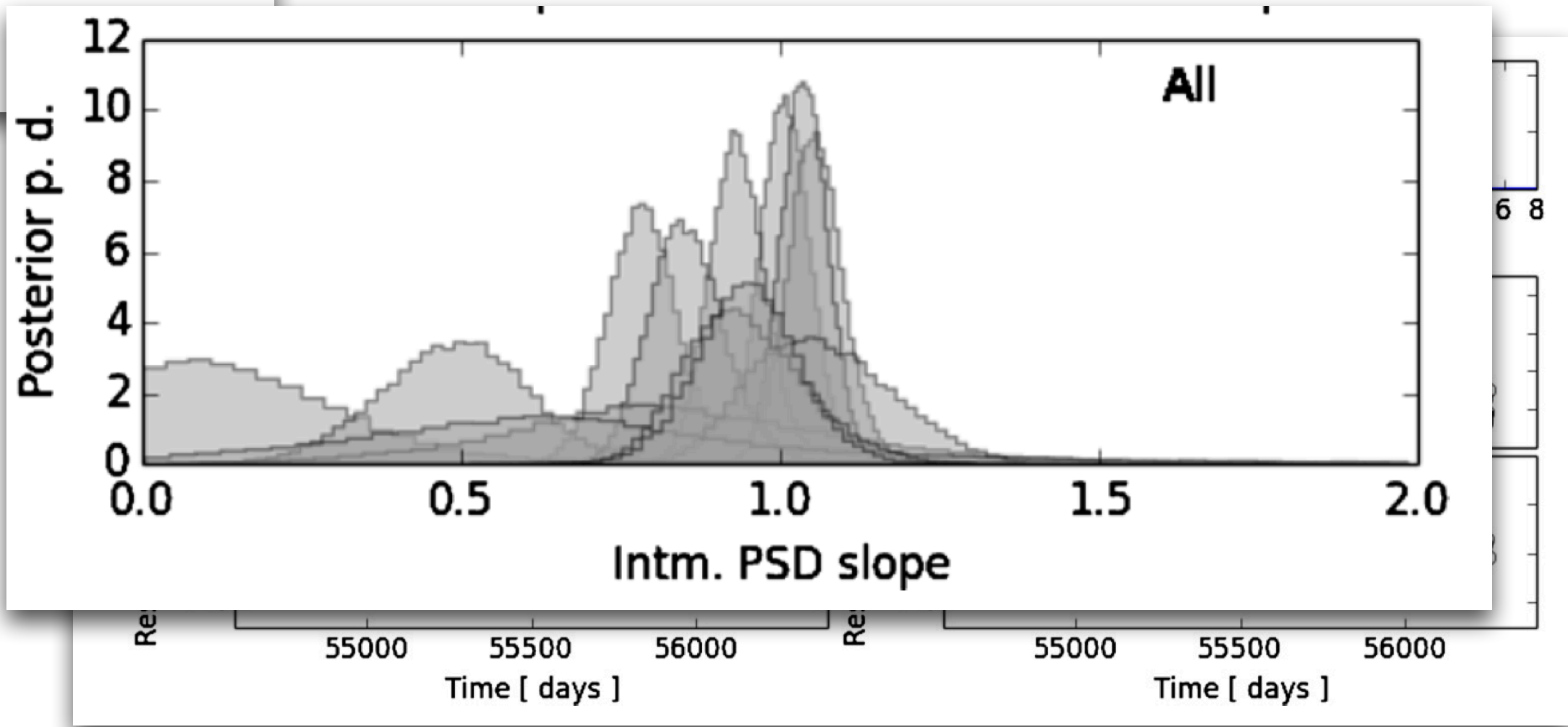

Pink versus Red Noise

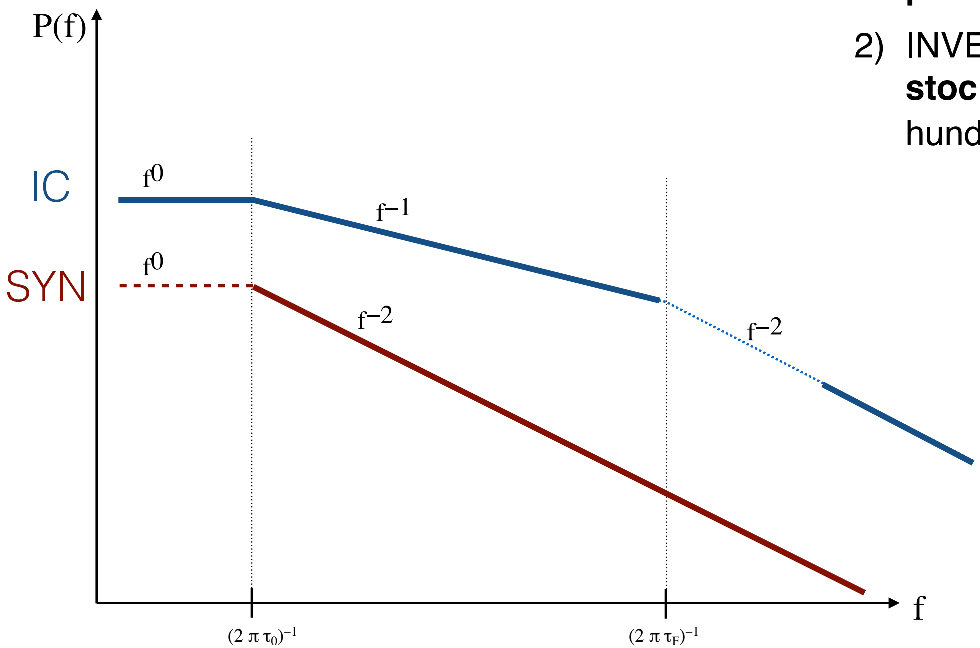

1) SYNCHROTRON: variability driven by an underlying **single stochastic process** with the relaxation timescale $\tau_0 > \mathrm{yrs}$
2) INVERSE-COMPTON: variability driven by **a linear superposition of stochastic processes** with relaxation timescales between $\tau_0 \sim$ hundreds days and $\tau_F < \mathrm{day}$

Pink versus Red Noise

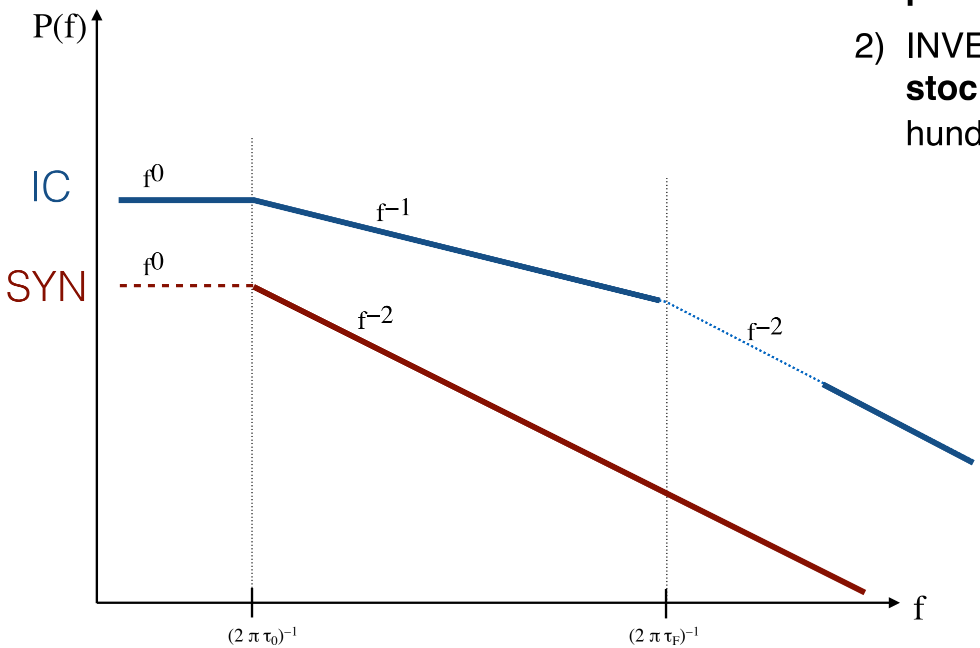

1) SYNCHROTRON: variability driven by an underlying **single stochastic process** with the relaxation timescale $\tau_0 > \mathrm{yrs}$
2) INVERSE-COMPTON: variability driven by **a linear superposition of stochastic processes** with relaxation timescales between $\tau_0 \sim$ hundreds days and $\tau_F < \mathrm{day}$

* relaxation timescales can be probed observationally and linked to the jet physics (but what is the meaning of a very long τ_0? maybe more related to accretion disk?)
* emission produced within extended segment of the jet, not a single well-defined "blazar emission zone"

Continuous Gamma-ray Monitoring!

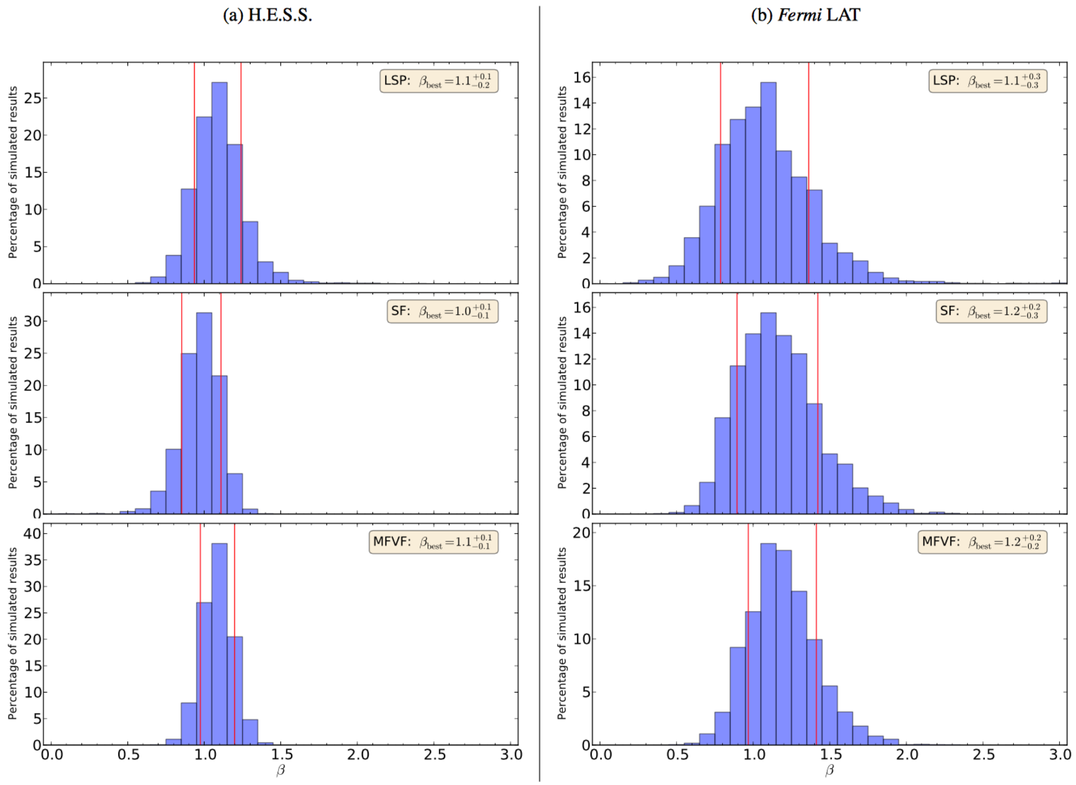

Abdalla et al. 2017
days to years
β~1

Aharonian et al. 2007
minutes-hours
β~2

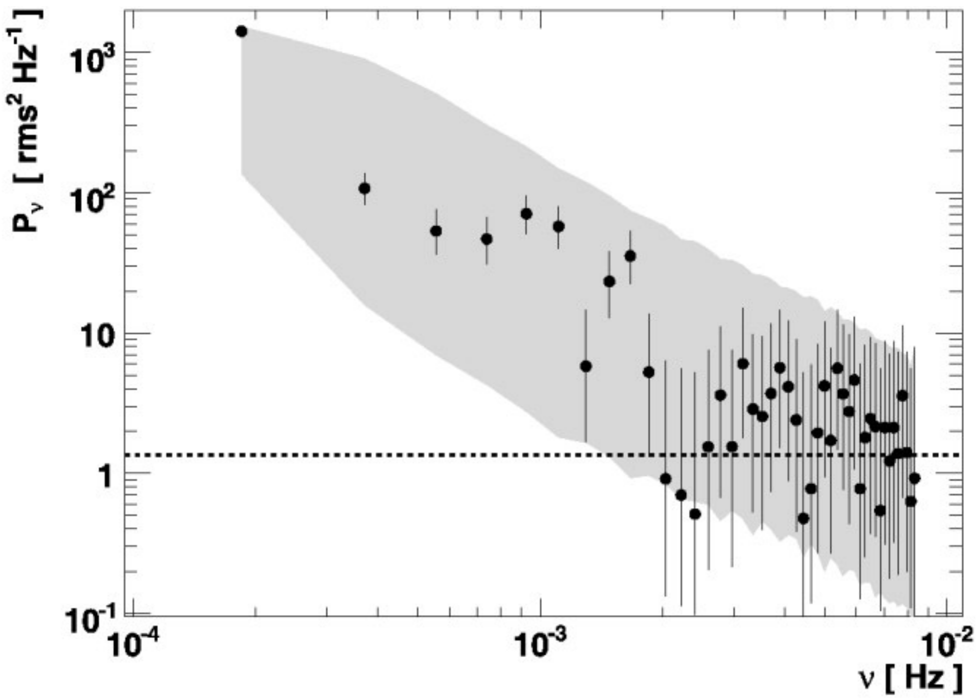

Continuous Stratified Jets

Zdziarski, LS, Sikora, 2019:
models for the MHD jet emission

model parameters: profiles

jet radius $R=R(z)$
bulk Lorentz factor $\Gamma=\Gamma(R, z)$
jet magnetic field $B=B(R, z)$
jet magnetization $\sigma=\sigma(R, z)$
electron injection $Q=Q(\gamma,R, z)$

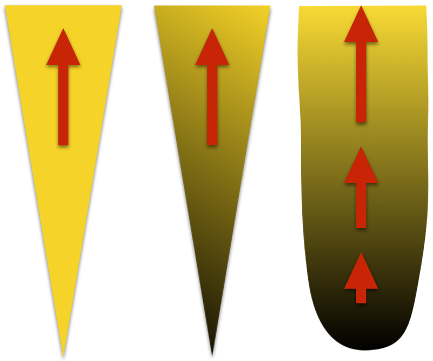

assumed electron injection spectrum Q

$$\frac{\partial \mathcal{N}_{\rm e}(\gamma,t)}{\partial t} = \frac{\partial}{\partial \gamma}\left\{|\dot{\gamma}|\, \mathcal{N}_{\rm e}(\gamma,t)\right\} + Q(\gamma,t)$$

Continuous Stratified Jets

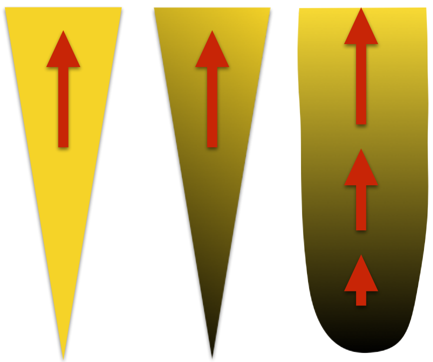

Zdziarski, LS, Sikora, 2019:
models for the MHD jet emission:

a) constant bulk velocity, free-expanding, particle-dominated jet, with the electron distribution maintained (by some unspecified dissipation process) along the outflow, and the magnetic field scaling according to the conservation of magnetic energy (Blandford & Konigl 1979)

b) as above, but with the evolving electron energy distribution calculated self-consistently (radiative and adiabatic losses) for a given (assumed) injection function

c) slowly collimating and accelerating MHD outflow (Komissarov et al., Lyubarsky, etc.) with the evolving electron energy distribution calculated self-consistently (radiative and adiabatic losses) for a given (assumed) injection function

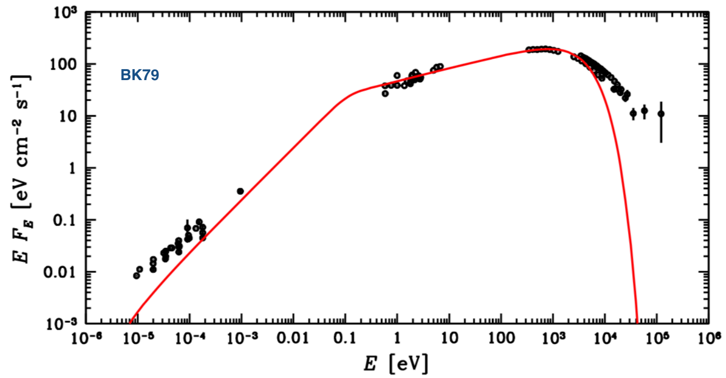

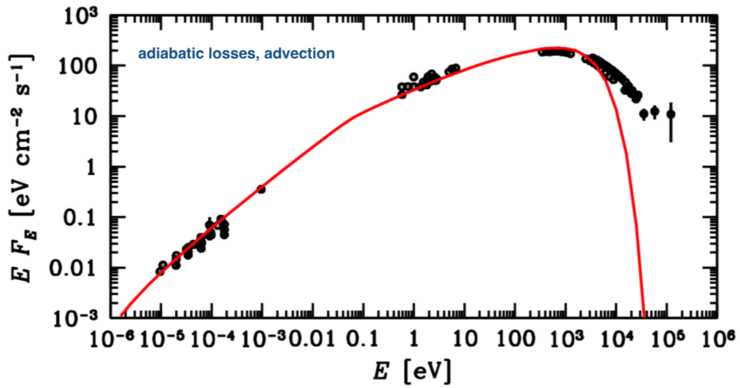

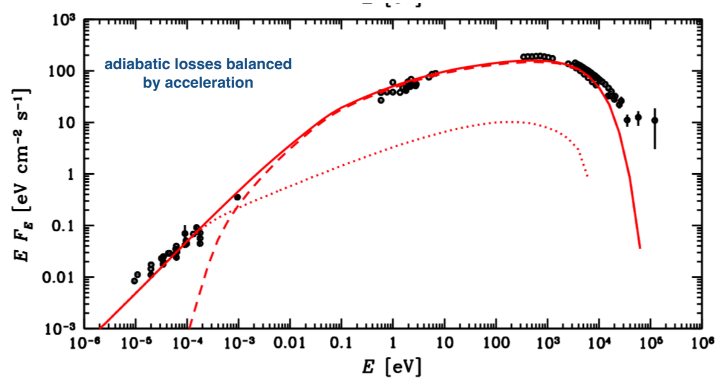

“We show that accounting for adiabatic losses in the case of sources showing soft partially self-absorbed spectra with the spectral index of a < 0 in the radio-to-IR regime requires deposition of large amounts of energy at large distances in the jet.”

Jet Magnetization

Lyubarsky (2010) showed that for various initial magnetic field configurations or external pressure profiles, jets could possibly cease to be Poynting-flux dominated only at logarithmically large distances from the jet base.

Efficiency of magnetic reconnection depends on the plasma magnetization (e.g., Sironi & Spitkovsky 2014)

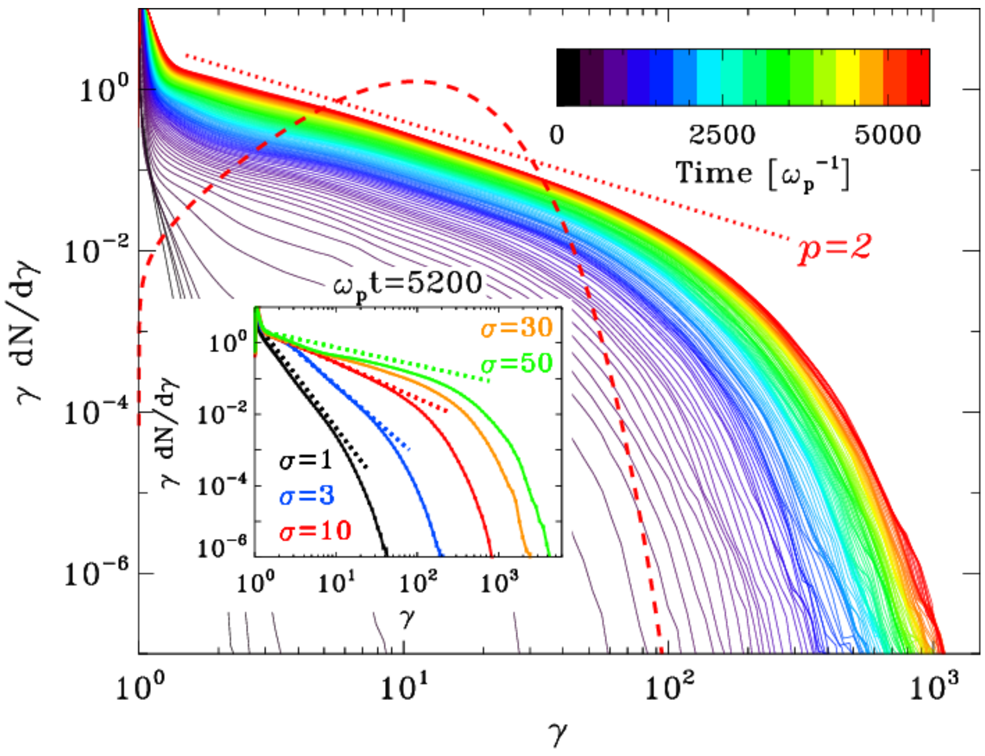

Jet Magnetization

Król, LS, et al. 2022

A simple analytical model for relativistic current-carrying jets at larger distances from their launching sites, assuming a cylindrical axi-symmetric geometry with a radial velocity shear, purely toroidal configuration for the jet magnetic field, and ultra-relativistic equation of state for the jet particles.

As long as the jet plasma is in **magnetohydrostatic equilibrium** $\overrightarrow{\nabla} P = \vec{J} \times \overrightarrow{B}$, and pressure radial profiles are continuous, such outflows have to be always particle dominated, in the sense that the ratio of the electromagnetic to particle energy fluxes integrated over the jet cross-section area, tends to be below unity, i.e. the jet magnetization parameter $\sigma < 1$.
At the same time, for particular magnetic and radial velocity profiles, magnetic pressure may still dominate over particle pressure for certain ranges of the jet radius, i.e. that the local jet plasma parameter $\beta_{\rm pl}^{-1} > 1$.

Jet may be globally magnetically dominated ($\sigma \gtrsim 1$) only in the case of huge pressure jumps/discontinuities at certain jet radii (by several orders of magnitude), and negligible velocity shear (essentially, a completely non-magnetised jet spine surrounded by a force-free boundary layer).

$$\boxed{\partial_r P = -\frac{1}{8\pi r^2}\;\partial_r\!\left(\frac{r^2 B_\phi^2}{\Gamma^2}\right)}$$

$$\boxed{\sigma \equiv \frac{L_B}{L_p} = \frac{1}{16\pi}\,\frac{\int dr\, r\,\beta\, B_\phi^2}{\int dr\, r\,\beta\,\Gamma^2\, P}}$$

Jet Magnetization

jet radius $x = r/R_\mathrm{j}$

normalized particle pressure p(x)

normalized magnetic pressure b(x)

normalized rest-frame magnetic pressure f(x),

jet bulk Lorentz factor $\Gamma(x)$

boundary condition $q = \beta_{\mathrm{pl}}^{-1}(1)$

$$\boxed{\beta_{\mathrm{pl}}^{-1}(x) \equiv \frac{P_B(x)}{P(x)}}$$

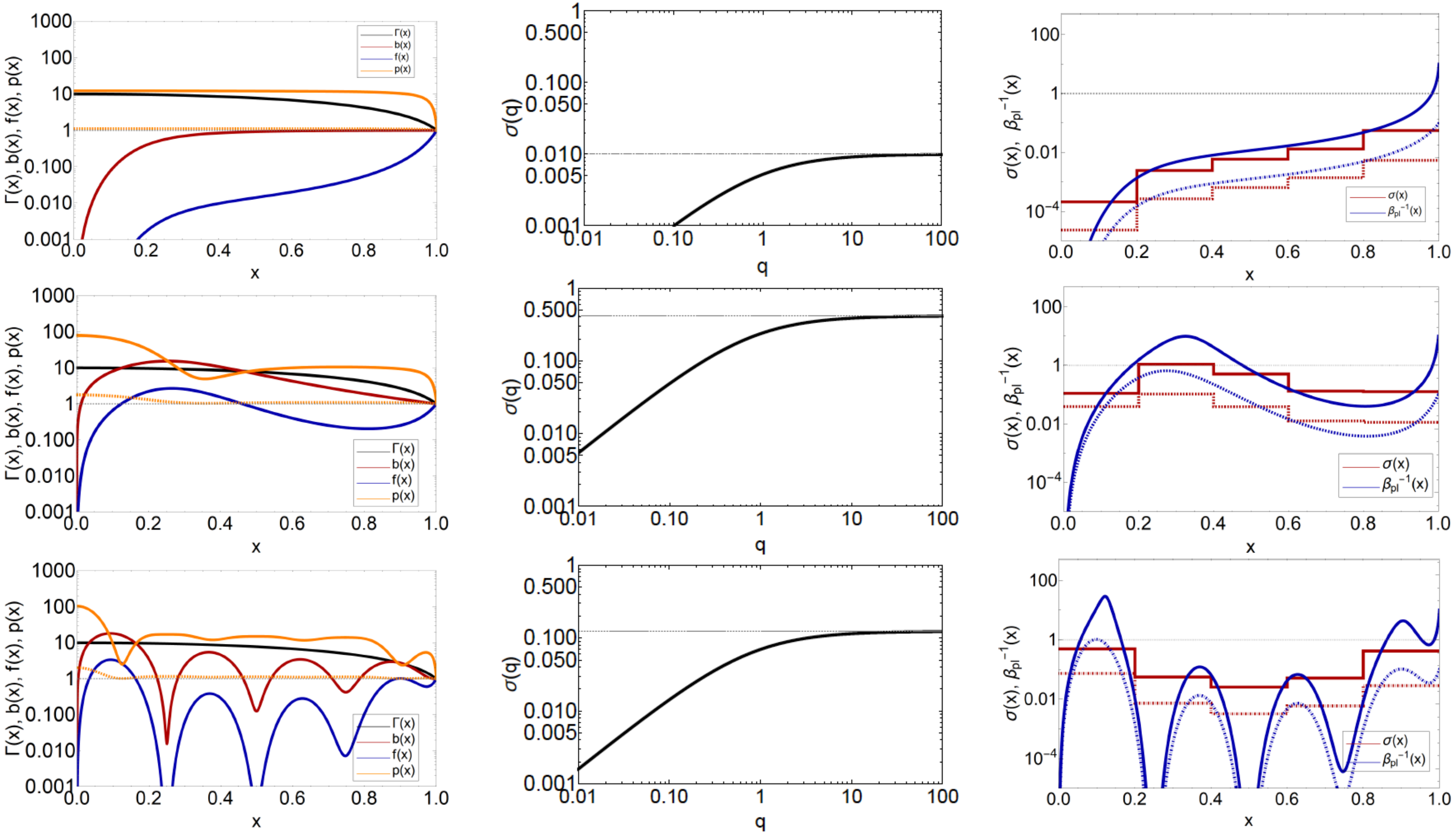

Król, LS, et al. 2022

Unstable, but…

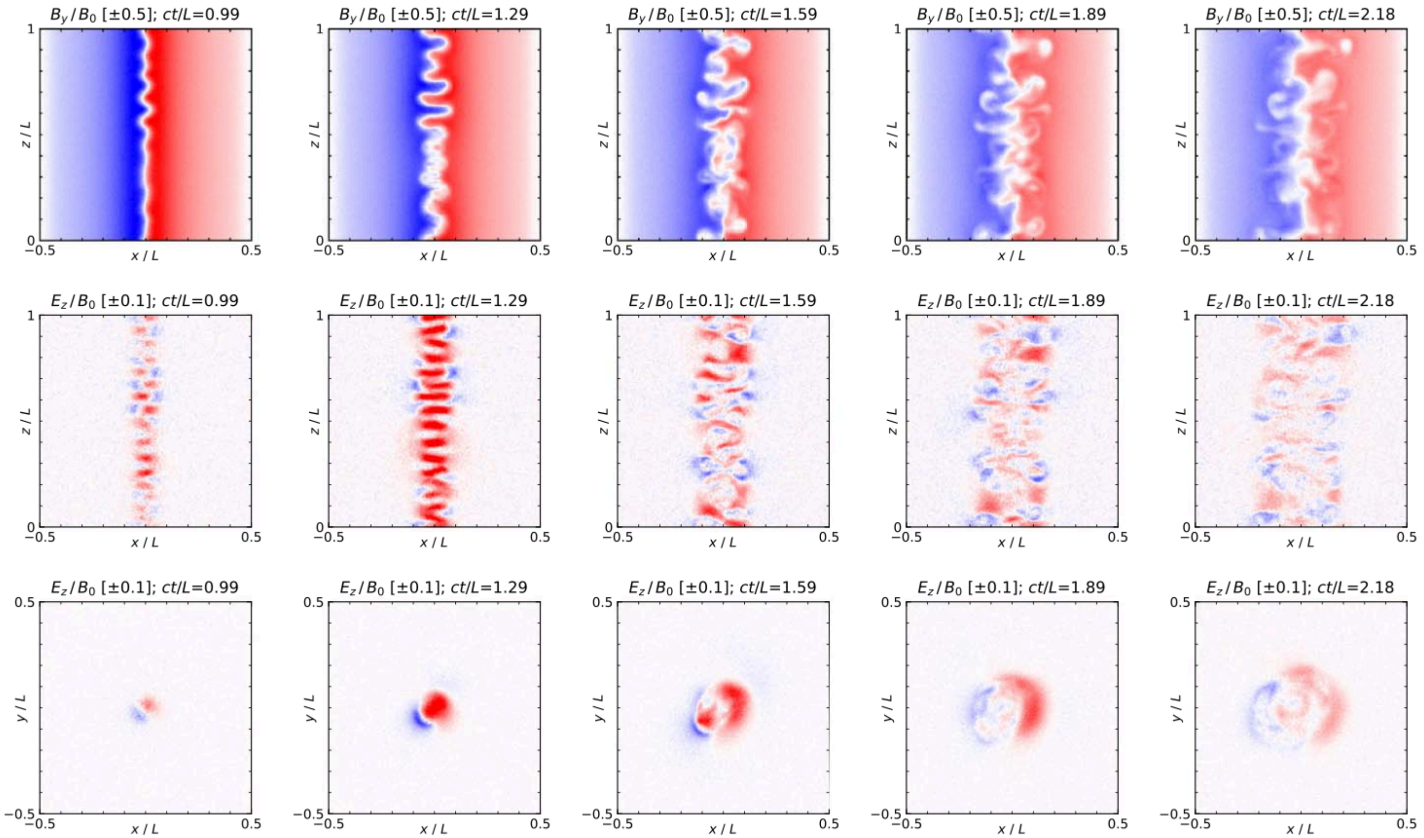

Figure 2. Maps of the magnetic field component B_y (top row of panels) and the electric field component E_z (middle row of panels) in the $y = 0$ plane, as well as the E_z component in the $z = 0$ plane (bottom row of panels), all in units of B_0 (positive values in red, negative in blue), at regular time intervals (from left to right) for the reference simulation f1_α-1_ξ10.

Ortuno-Mcias et al. 2022:

During the nonlinear development of the instabilities, a large-scale induced coherent electric field appears in the axial direction, enabling for an efficient acceleration of the jet particles up to the Hillas limit.

Termination Shocks

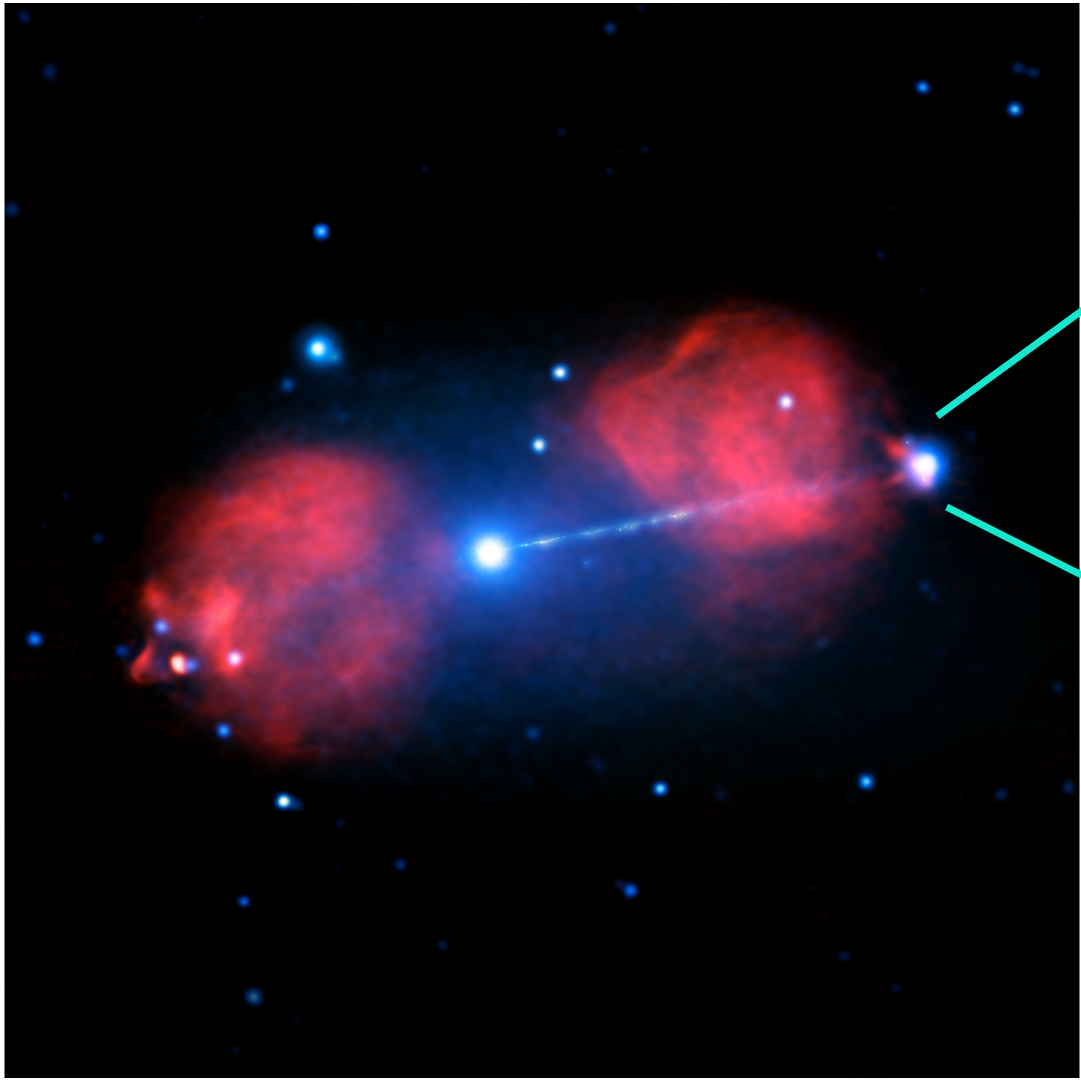

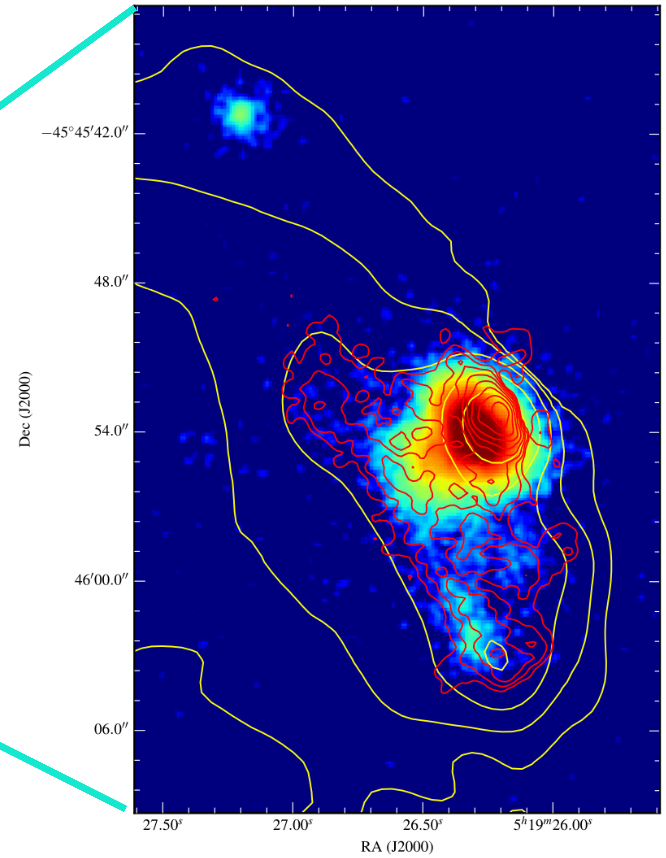

<u>Hardcastle et al. 2016:</u>
deep Chandra observations (~0.5 Ms)
of the radio galaxy Pictor A

Termination Shocks

Thimmappa, LS, et al. 2020:
re-analysis of the Chandra data
& image deconvolution

Table 1
Observational Data and Spectral Fitting Results

ObsID	Date	MJD	Exposure (ks)	θ (arcmin)	Γ	red.χ^2	$F_{0.5-7.0\ \mathrm{keV}}$ (10^{-13} erg cm^{-2} s^{-1})	Counts[a]
346	2000-01-18	51561	25.8	3.50	2.01 ± 0.05	0.272	5.41 (+0.20/−0.45)	3461
3090	2002-09-17	52534	46.4	0.11	1.96 ± 0.03	0.377	5.64 (+0.03/−0.20)	5278
4369	2002-09-22	52539	49.1	0.11	1.99 ± 0.03	0.426	5.61 (+0.11/−0.15)	5564
12039	2009-12-07	55172	23.7	3.35	1.98 ± 0.06	0.260	5.71 (+0.02/−0.10)	2290
12040	2009-12-09	55174	17.3	3.35	2.07 ± 0.08	0.265	5.47 (+0.08/−0.25)	1710
11586	2009-12-12	55177	14.3	3.35	2.11 ± 0.09	0.212	5.39 (+0.21/−0.40)	1427
14357	2012-06-17	56095	49.3	3.07	2.05 ± 0.05	0.321	5.88 (+0.06/−0.14)	3043
14221	2012-11-06	56237	37.5	3.10	2.08 ± 0.05	0.356	5.84 (+0.01/−0.11)	3248
15580	2012-11-08	56239	10.5	3.10	2.08 ± 0.14	0.235	5.24 (+0.30/−0.21)	935
14222	2014-01-17	56674	45.4	3.30	2.00 ± 0.05	0.329	5.78 (+0.12/−0.10)	3428
16478	2015-01-09	57031	26.8	3.32	1.95 ± 0.08	0.232	5.30 (+0.15/−0.54)	1657
17574	2015-01-10	57032	18.6	3.32	2.04 ± 0.11	0.209	5.33 (+0.26/−0.21)	1187

Note.
[a] Total number of counts within the 0.5–7.0 keV range from a circular region with a radius 20 px centered on the hotspot.

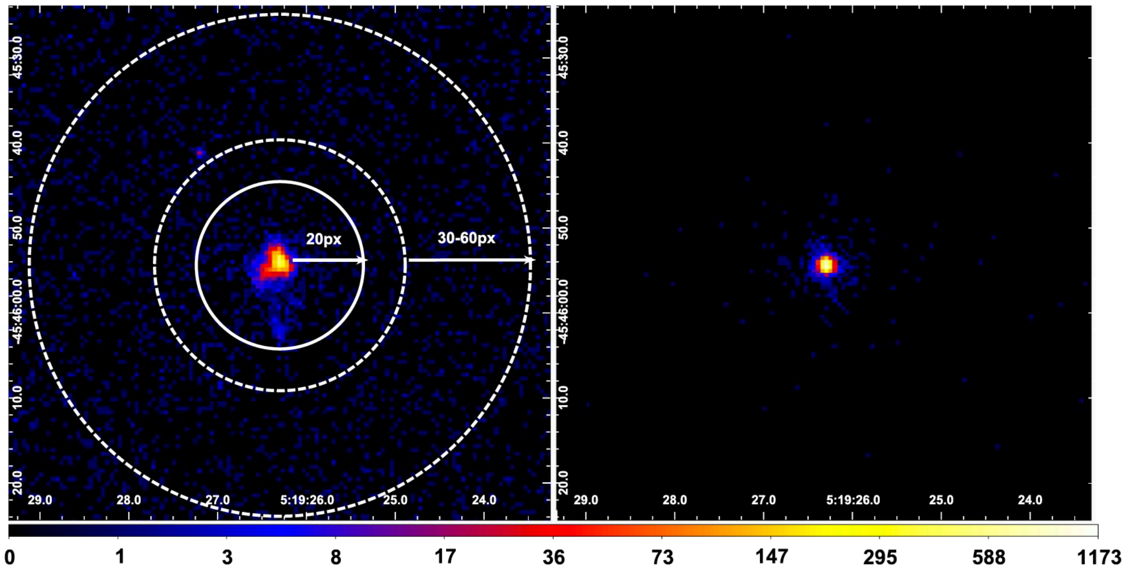

Termination Shocks

Table 1
Observational Data and Spectral Fitting Results

ObsID	Date	MJD	Exposure (ks)	θ (arcmin)	Γ	red.χ^2	$F_{0.5-7.0\ \mathrm{keV}}$ (10^{-13} erg cm^{-2} s^{-1})	Counts[a]
346	2000-01-18	51561	25.8	3.50	2.01 ± 0.05	0.272	5.41 (+0.20/−0.45)	3461
3090	2002-09-17	52534	46.4	0.11	1.96 ± 0.03	0.377	5.64 (+0.03/−0.20)	5278
4369	2002-09-22	52539	49.1	0.11	1.99 ± 0.03	0.426	5.61 (+0.11/−0.15)	5564
12039	2009-12-07	55172	23.7	3.35	1.98 ± 0.06	0.260	5.71 (+0.02/−0.10)	2290
12040	2009-12-09	55174	17.3	3.35	2.07 ± 0.08	0.265	5.47 (+0.08/−0.25)	1710
11586	2009-12-12	55177	14.3	3.35	2.11 ± 0.09	0.212	5.39 (+0.21/−0.40)	1427
14357	2012-06-17	56095	49.3	3.07	2.05 ± 0.05	0.321	5.88 (+0.06/−0.14)	3043
14221	2012-11-06	56237	37.5	3.10	2.08 ± 0.05	0.356	5.84 (+0.01/−0.11)	3248
15580	2012-11-08	56239	10.5	3.10	2.08 ± 0.14	0.235	5.24 (+0.30/−0.21)	935
14222	2014-01-17	56674	45.4	3.30	2.00 ± 0.05	0.329	5.78 (+0.12/−0.10)	3428
16478	2015-01-09	57031	26.8	3.32	1.95 ± 0.08	0.232	5.30 (+0.15/−0.54)	1657
17574	2015-01-10	57032	18.6	3.32	2.04 ± 0.11	0.209	5.33 (+0.26/−0.21)	1187

Note.
[a] Total number of counts within the 0.5–7.0 keV range from a circular region with a radius 20 px centered on the hotspot.

Thimmappa, LS, et al. 2020:
re-analysis of the Chandra data
& image deconvolution

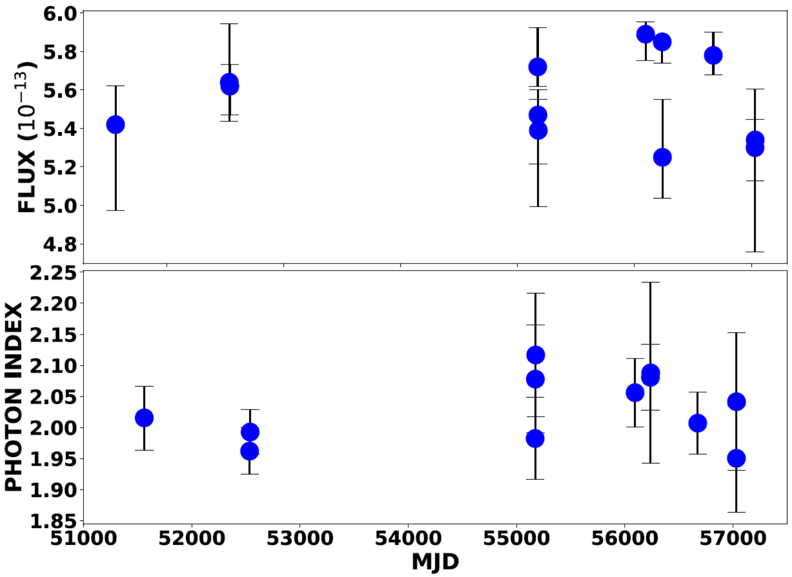

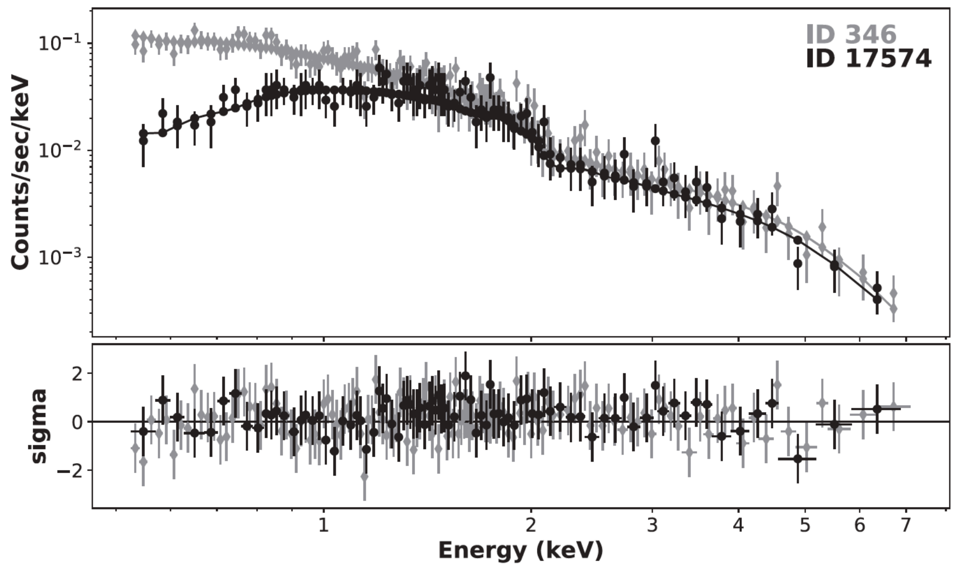

Termination Shocks

Thimmappa, LS, et al. 2020:
re-analysis of the Chandra data
& image deconvolution

Table 1
Observational Data and Spectral Fitting Results

ObsID	Date	MJD	Exposure (ks)	θ (arcmin)	Γ	red.χ^2	$F_{0.5-7.0\,\mathrm{keV}}$ (10^{-13} erg cm^{-2} s^{-1})	Counts[a]
346	2000-01-18	51561	25.8	3.50	2.01 ± 0.05	0.272	5.41 (+0.20/−0.45)	3461
3090	2002-09-17	52534	46.4	0.11	1.96 ± 0.03	0.377	5.64 (+0.03/−0.20)	5278
4369	2002-09-22	52539	49.1	0.11	1.99 ± 0.03	0.426	5.61 (+0.11/−0.15)	5564
12039	2009-12-07	55172	23.7	3.35	1.98 ± 0.06	0.260	5.71 (+0.02/−0.10)	2290
12040	2009-12-09	55174	17.3	3.35	2.07 ± 0.08	0.265	5.47 (+0.08/−0.25)	1710
11586	2009-12-12	55177	14.3	3.35	2.11 ± 0.09	0.212	5.39 (+0.21/−0.40)	1427
14357	2012-06-17	56095	49.3	3.07	2.05 ± 0.05	0.321	5.88 (+0.06/−0.14)	3043
14221	2012-11-06	56237	37.5	3.10	2.08 ± 0.05	0.356	5.84 (+0.01/−0.11)	3248
15580	2012-11-08	56239	10.5	3.10	2.08 ± 0.14	0.235	5.24 (+0.30/−0.21)	935
14222	2014-01-17	56674	45.4	3.30	2.00 ± 0.05	0.329	5.78 (+0.12/−0.10)	3428
16478	2015-01-09	57031	26.8	3.32	1.95 ± 0.08	0.232	5.30 (+0.15/−0.54)	1657
17574	2015-01-10	57032	18.6	3.32	2.04 ± 0.11	0.209	5.33 (+0.26/−0.21)	1187

Note.
[a] Total number of counts within the 0.5–7.0 keV range from a circular region with a radius 20 px centered on the hotspot.

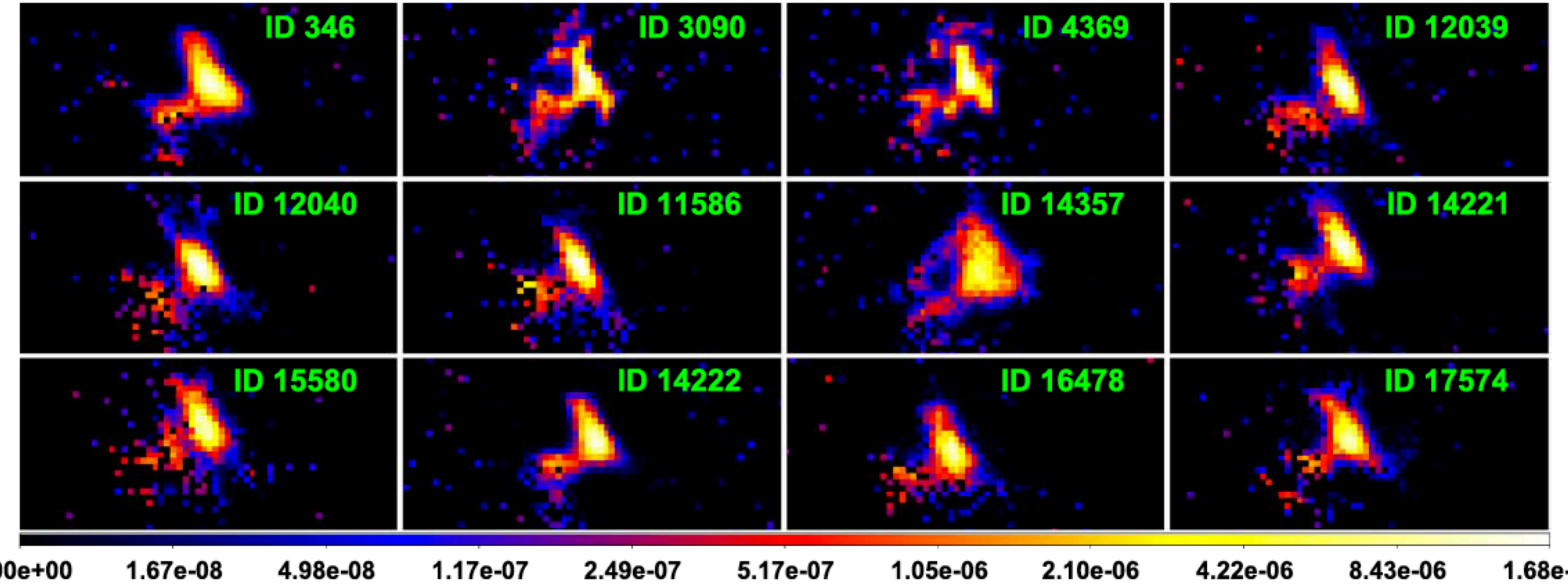

Figure 6. Deconvolved Chandra images of the W hotspot in Pictor A at 0.5 px resolution. Each image results from averaging over the restored images for 100 PSF realizations using the LRDA on the exposure-corrected maps. The color scale gives the count rate (cts s^{-1}).

Termination Shocks

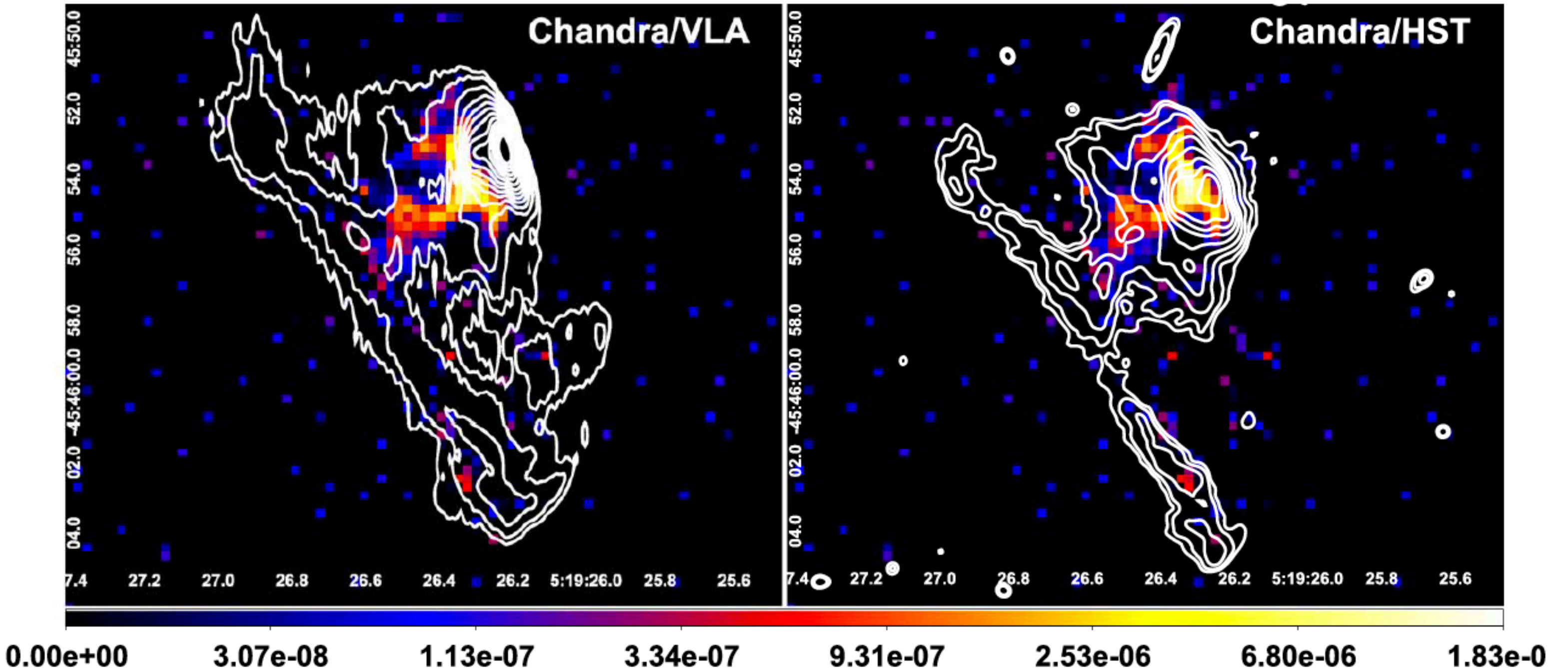

Figure 7. Deconvolved exposure-corrected Chandra image of the W hotspot in Pictor A at 0.5 px resolution for the ObsID 3090, averaged over 100 random realizations of the PSF, with the radio (3.6 cm wavelength, beam size 0.″77 × 0.″17, position angle −0.°4) VLA contours superimposed (left panel) and optical F606W filter (5918 Å, 90% encircled energy within radius 0.″35) Hubble Space Telescope ACS/WFC contours superimposed (right panel). Radio contours are spaced with a factor of $\sqrt{2}$ between 0.552% and 70.71% of the peak intensity of 215 mJy beam^{-1}. Optical contours are spaced with a factor of $\sqrt{2}$ between 0.008 and 3 cts s^{-1}.

Thimmappa, LS, et al. 2020:
we were able to resolve the X-ray structure of the hotspot into (i) the jet-like feature located in between the radio/optical filament and the termination shock, and (ii) the disk-like or conical feature perpendicular to the jet axis, and located ~1 kpc upstream the intensity peak of the radio hotspot. We believe that this later feature — resolved in its longitudinal direction to be ~3 kpc long, while remaining basically unresolved in its transverse direction, with the corresponding scale upper limit of < 200 pc — marks the position of the reverse shock front in the system, where efficient particle acceleration takes place.

Spectral Analysis

Problems:

* large extraction region for th spectral analysis -> integrated spectrum of the entire hotspot structure on the scales of arc seconds ~ kiloparsecs
* energy-dependent Chandra PSF and limited photon statistics both prohibit any more in-depth analysis

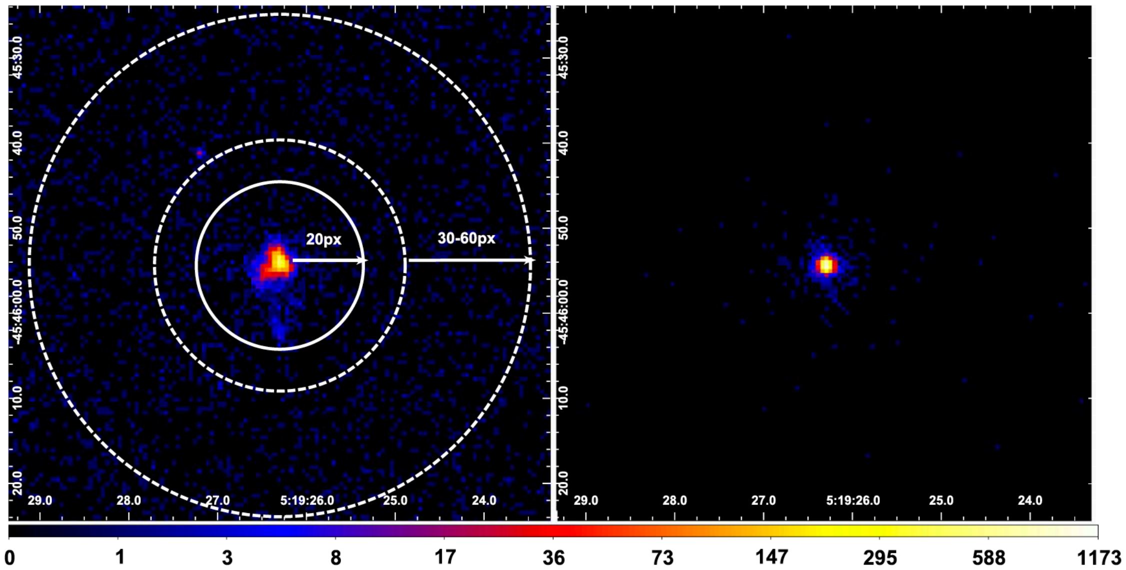

Spectral Analysis

Problems:

* large extraction region for th spectral analysis -> integrated spectrum of the entire hotspot structure on the scales of arc seconds ~ kiloparsecs
* energy-dependent Chandra PSF and limited photon statistics both prohibit any more in-depth analysis
* **but how about doing spatially-resolved spectroscopy based on deconvolve images in soft and hard bands?**

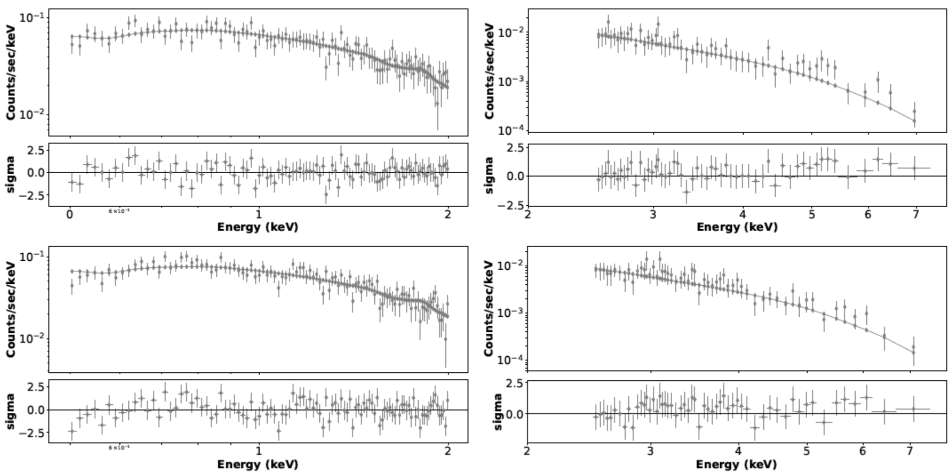

Table 1. Observational data and spectral fitting results for the soft (0.5 – 2.0 keV) and hard (2.5 – 7.0 keV) bands.

ObsID	Date	Exposure	Band	Count rate	Photon index	χ^2/dof	Energy flux	Net counts
		[ksec]		[cts/s]	Γ		$[10^{-13}\,\mathrm{erg\,cm^{-2}\,s^{-1}}]$	
3090	2002-09-17	46.4	soft	0.078	1.89 ± 0.05	0.727	$2.93^{+0.08}_{-0.05}$	3649
			hard	0.013	2.80 ± 0.40	0.208	$1.73^{+0.05}_{-0.12}$	906
4369	2002-09-22	49.1	soft	0.079	1.94 ± 0.05	0.964	$2.93^{+0.04}_{-0.03}$	3894
			hard	0.018	2.69 ± 0.36	0.233	$1.78^{+0.14}_{-0.29}$	924

<u>Thimmappa, LS, et al. 2022:</u>

Spectral Analysis

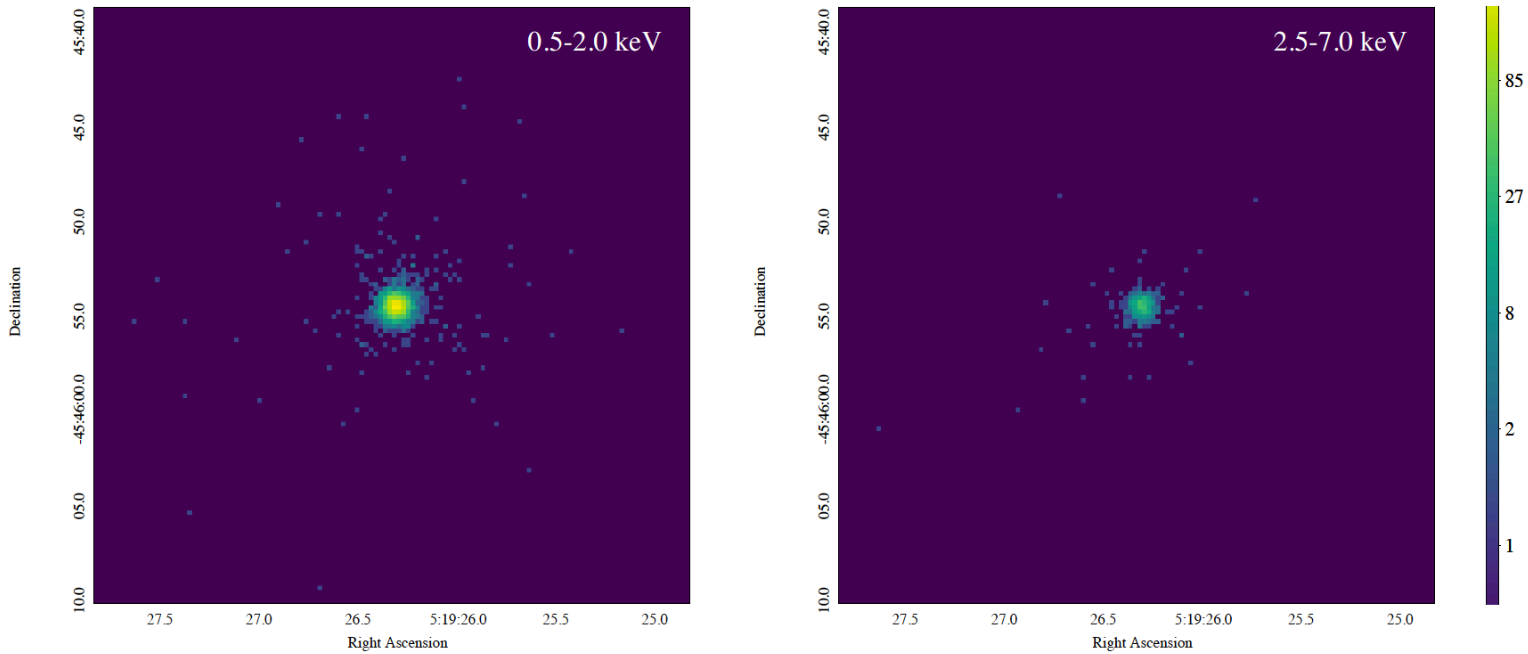

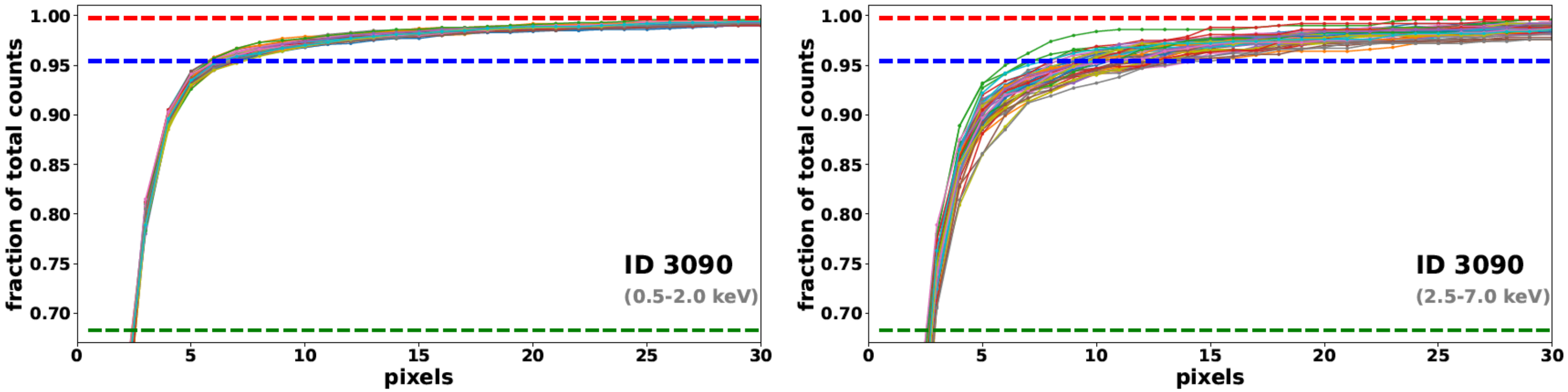

Thimmappa, LS, et al. 2022:

Resolved Spectroscopy

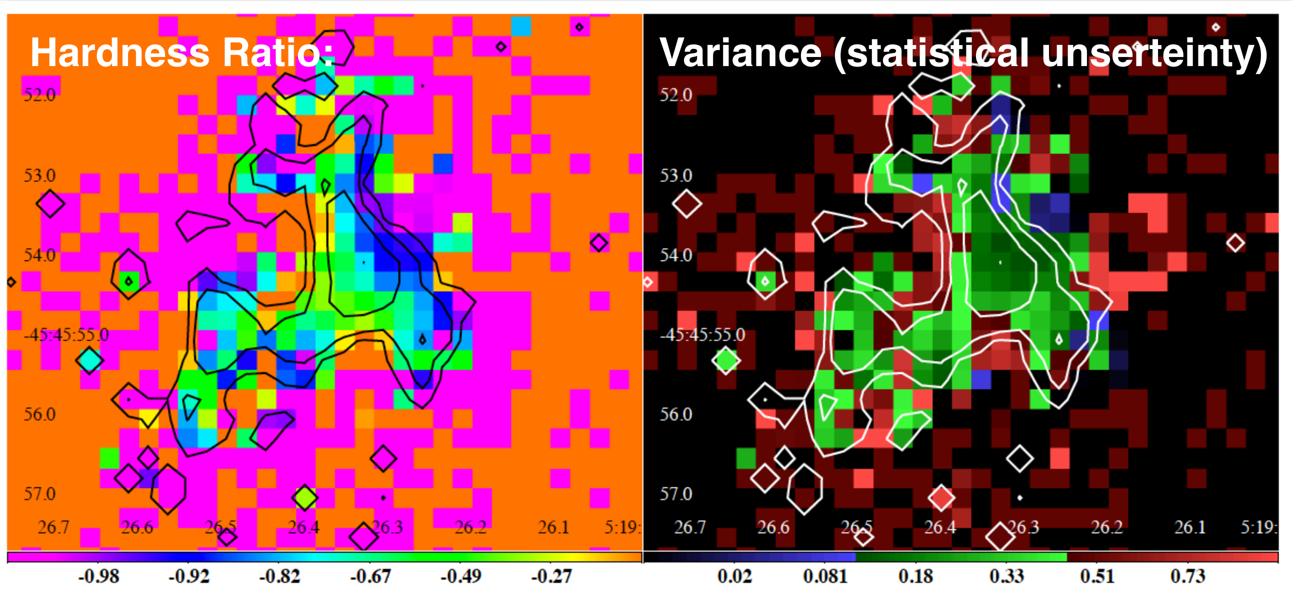

Thimmappa, LS, et al. 2022:

Resolved Spectroscopy

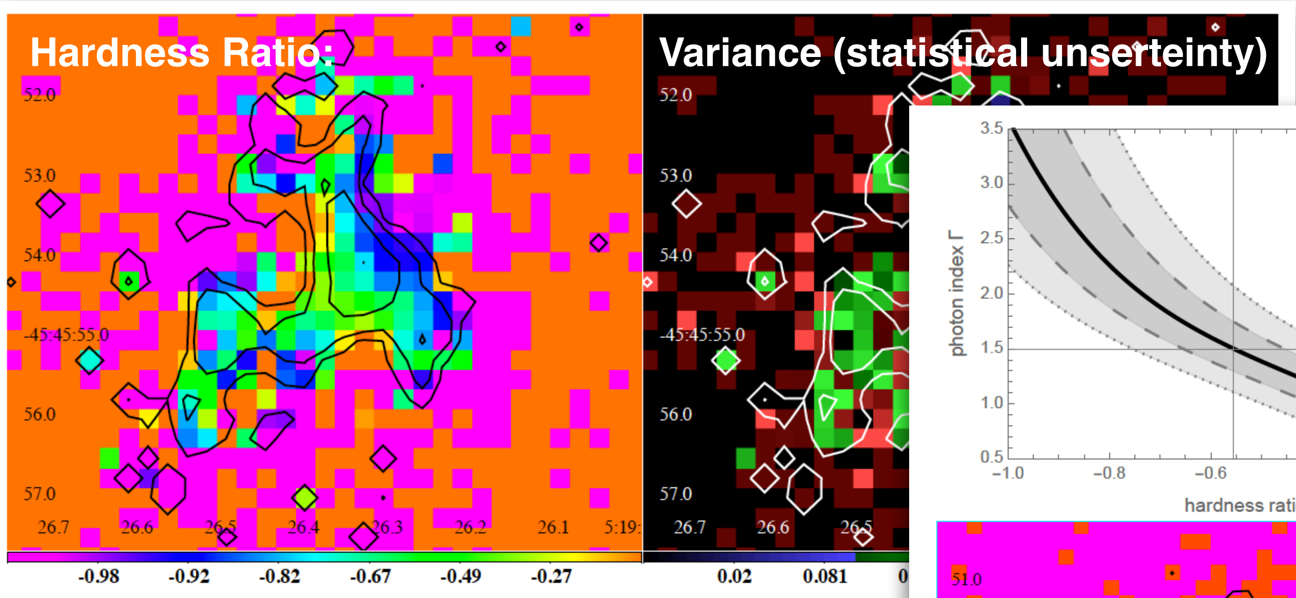

Thimmappa, LS, et al. 2022:

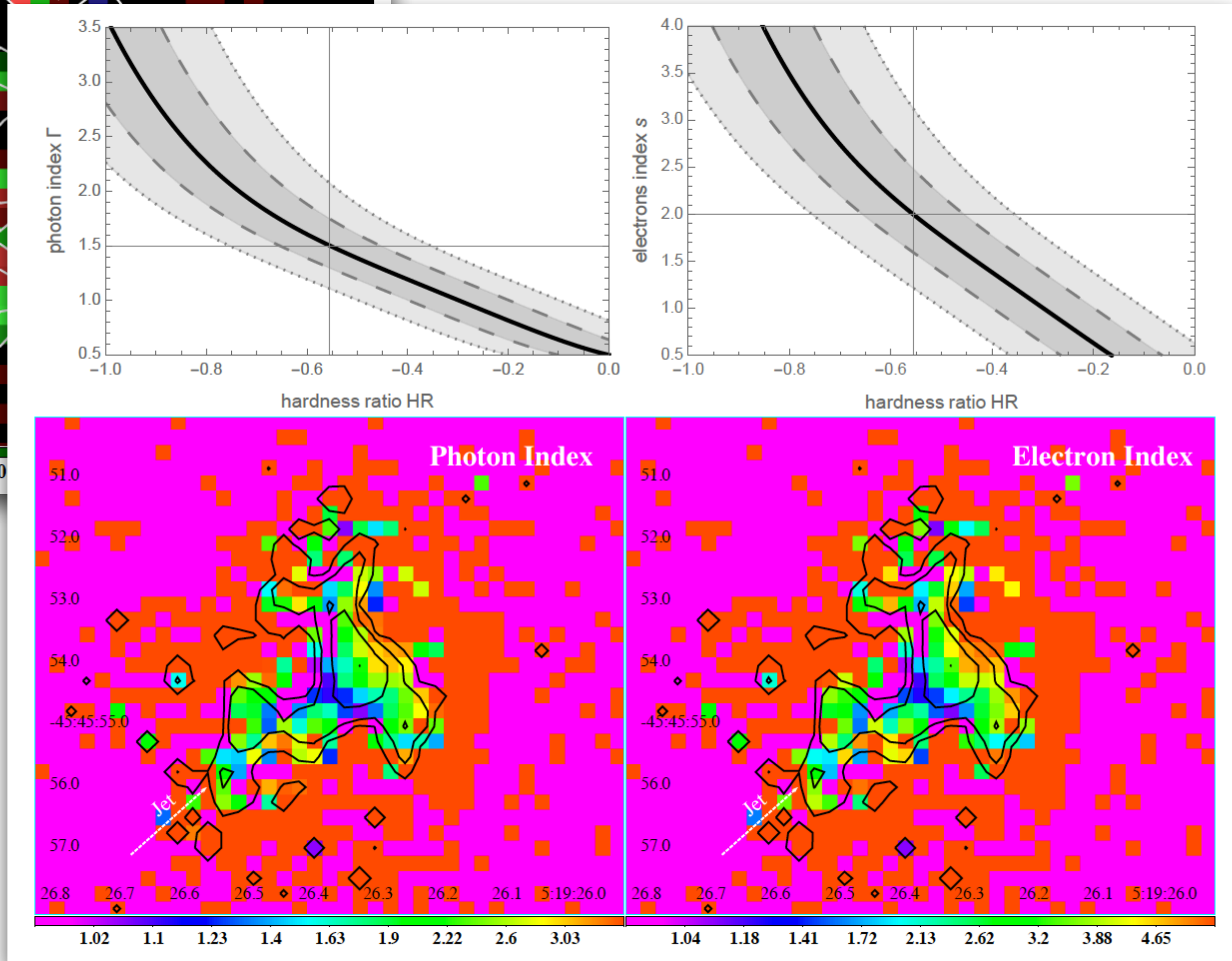

Resolved Spectroscopy

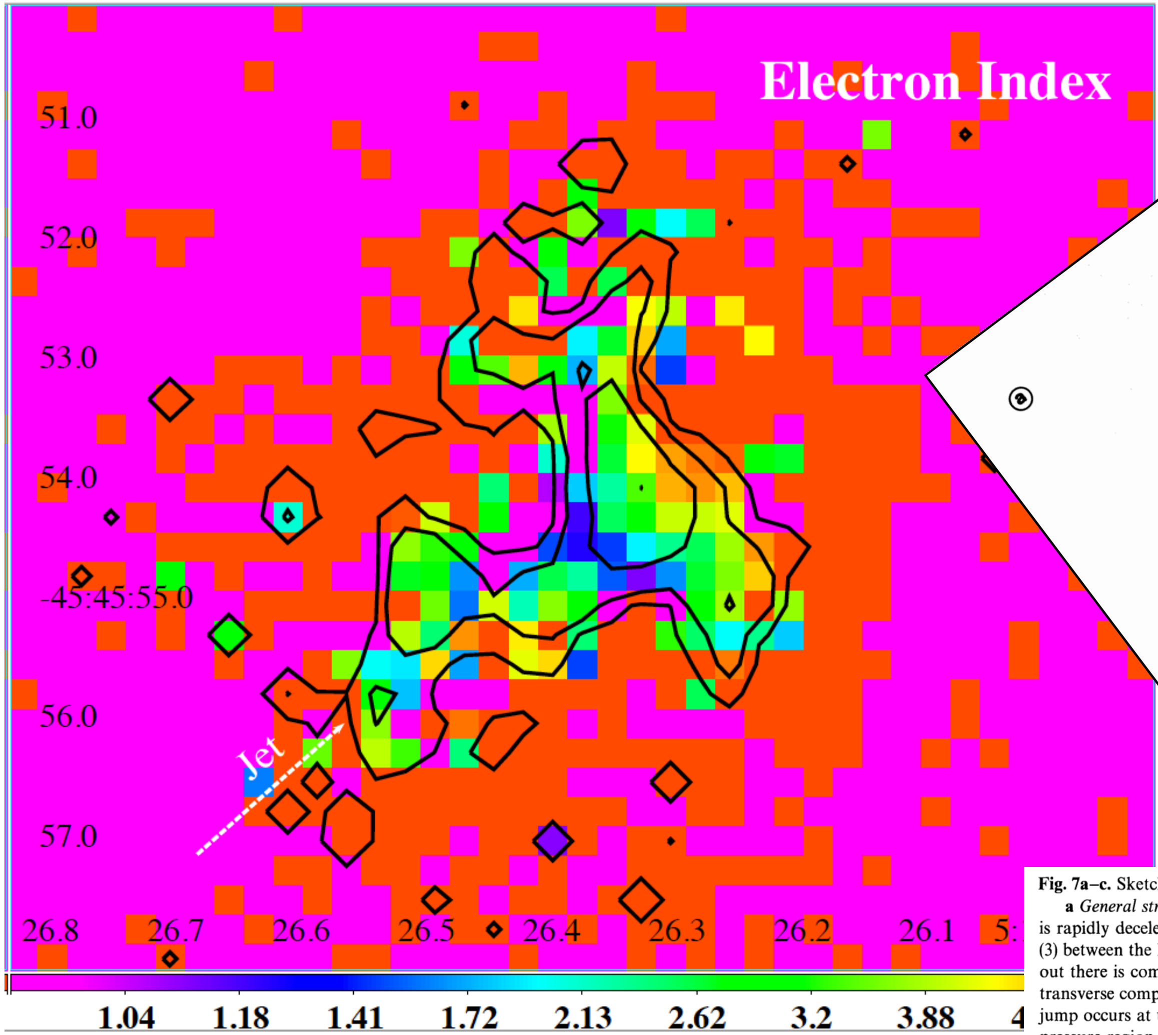

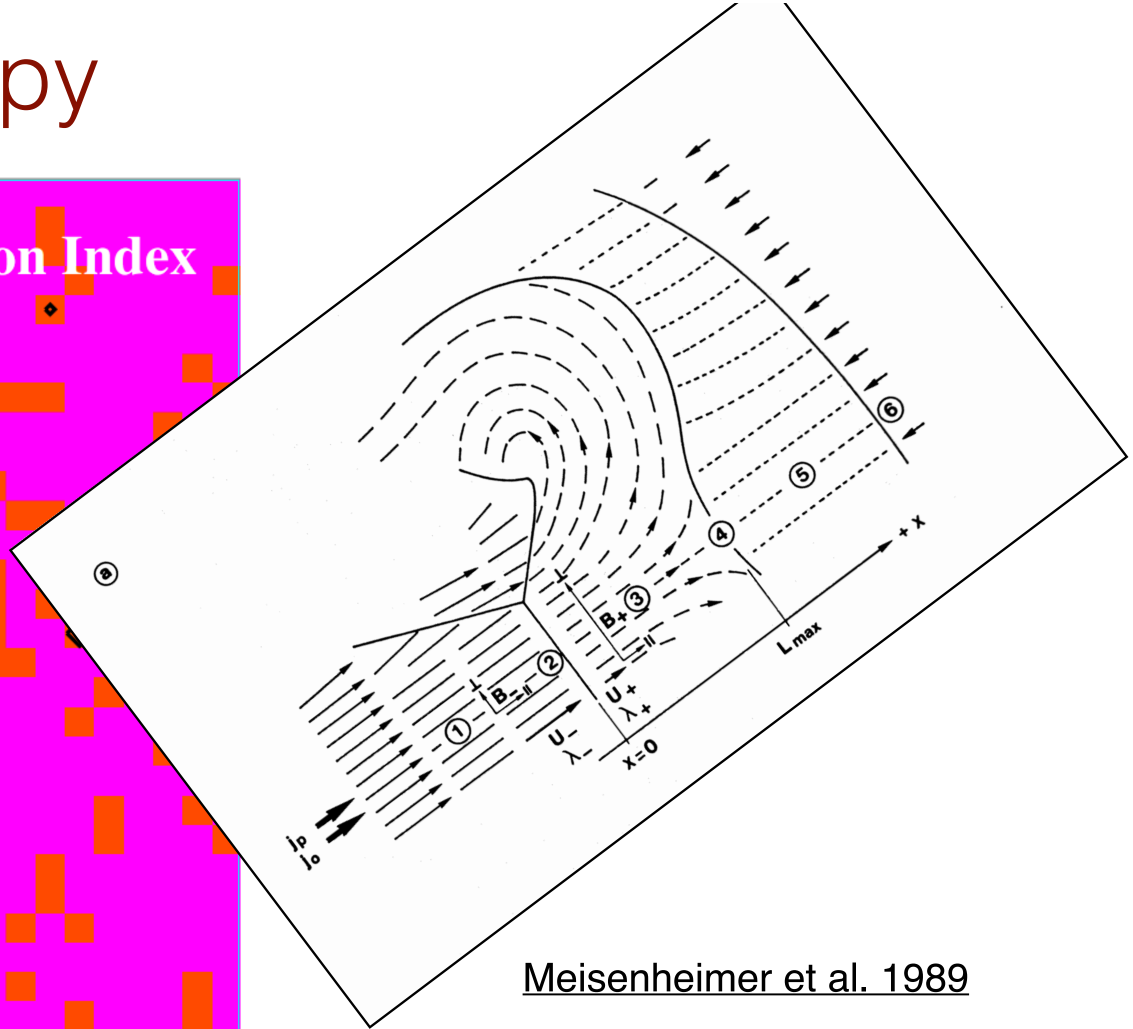

Meisenheimer et al. 1989

Fig. 7a–c. Sketch of the shock structure, flow pattern and magnetic field configuration in the beamhead of a supersonic jet.

a *General structure.* The jet (1) carries a flux of j_p protons and j_0 *relativistic* electrons toward the working surface. At the Mach disk (2) the flow is rapidly decelerated from u_- to u_+ and both the plasma density and the transverse field increase by at least $r = u_-/u_+$. The downstream region (3) between the Mach disk and the stagnation point (4) is characterized by further deceleration and a sideways bend of the velocity vectors. Further out there is compressed outer material (5) and a second outer "bow" shock (6). Note the triple shock structure near the Mach disk. Since only the transverse component $B_\perp$ is enhanced in the downstream region the mean field may flip from $B \parallel$ jet to $B \perp$ jet at the Mach disk. The largest velocity jump occurs at the Mach disk where the flow pattern is essentially one-dimensional. The hot-spot *emission region* is probably confined to the over-pressure region between the Mach disk and the stagnation point (maximum length: L_{max}).

Very High Energy Electrons!

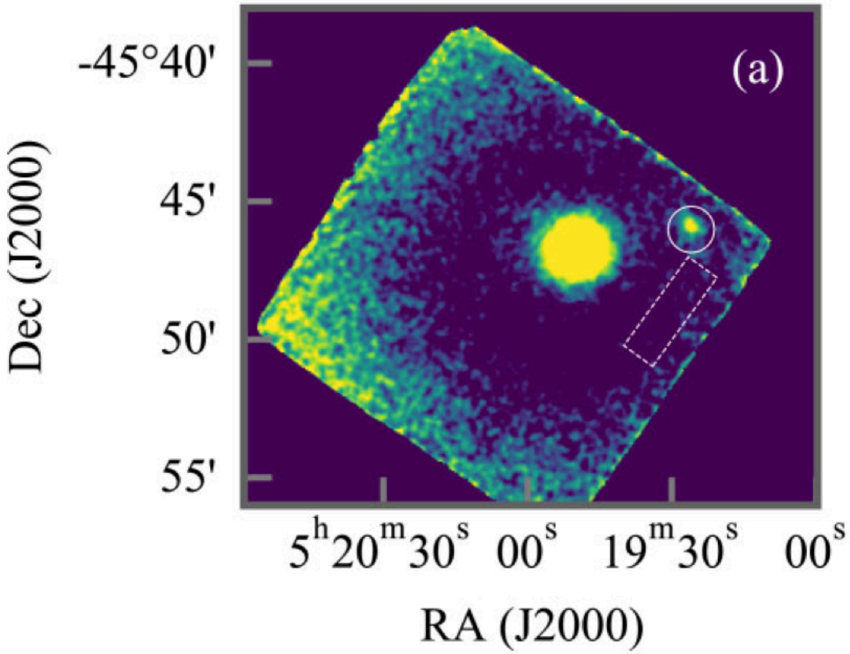

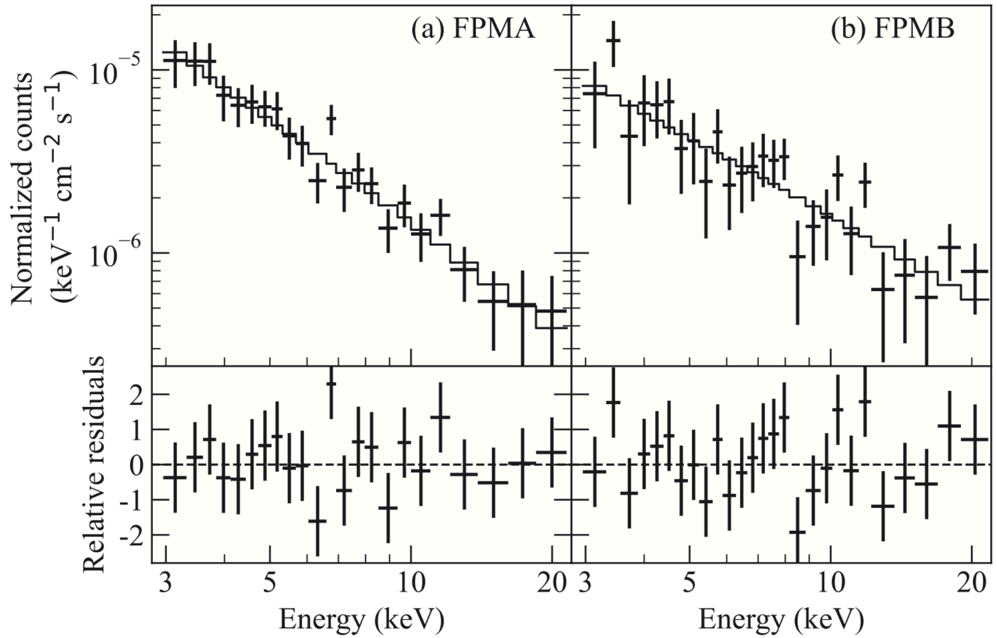

Sunada et al. 2022 - NuSTAR detection of Pictor A jet termination shocks

$$E_{\mathrm{e,max}} \simeq 40 \times \left(\frac{E_{\mathrm{cut}}}{20\ \mathrm{keV}}\right)^{1/2} \left(\frac{B}{300\ \mu\mathrm{G}}\right)^{-1}\ \mathrm{TeV}.$$

Very High Energy Electrons!

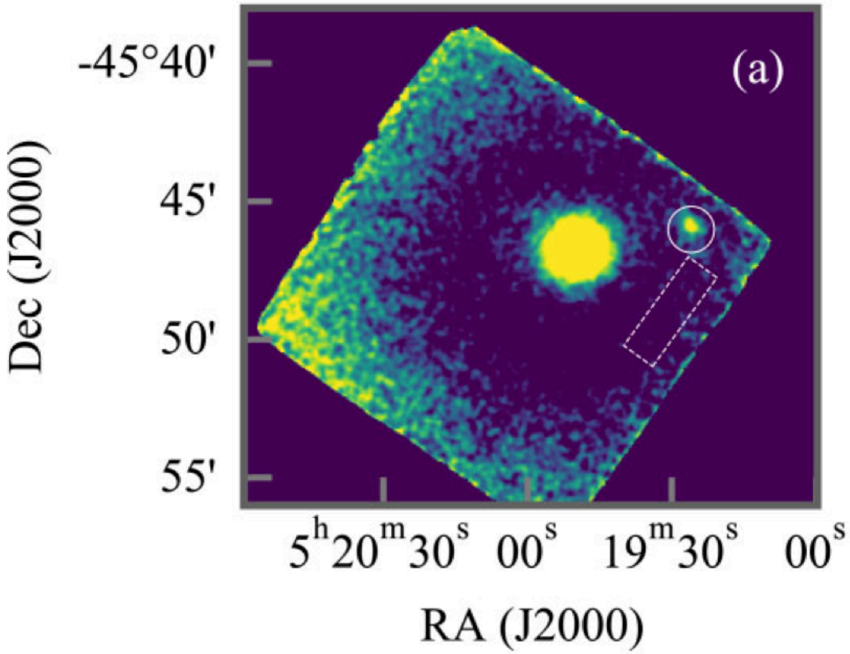

Sunada et al. 2022 - NuSTAR detection of Pictor A jet termination shocks

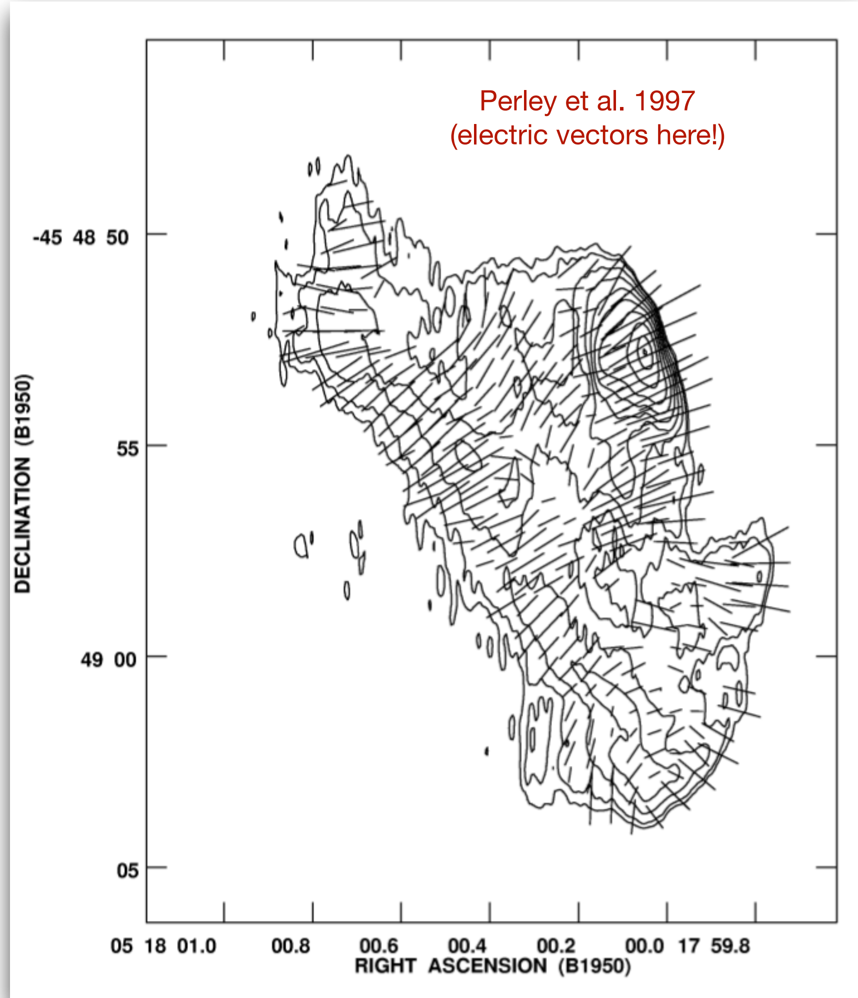

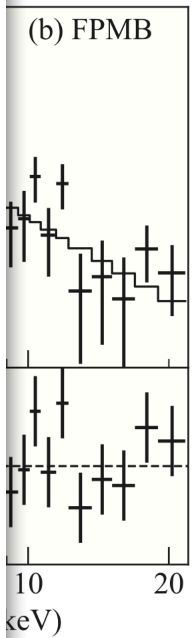

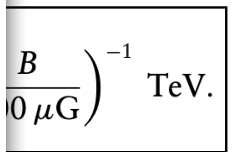

Conclusions

Particle acceleration in relativistic jets

- Blazar variability: pink and red noise, but what exactly does it tell us? relaxation timescales; extended stratified emission region
- Large-scale jets: magnetised boundary layers, co-axial electric field, stratification of the jet magnetization accross the outflow despite overall low magnetization
- Termination shocks: mildly-relativistic perpendicular shocks are very efficient electron accelerators up to at least 10—100 TeV energies!